Measurement of Neutral Mesons in p-Pb collisions at $\sqrt{s_{NN}} = 8.16$TeV with the ALICE detector

Author:
Samah AHMED

Supervisor:
Dr.Thomas DIETEL

A thesis submitted in fulfillment of the requirements for the degree of MASTER THESIS

August 30, 2019

Abstract

The measured transverse momentum spectra of neutral pion π^0 and η mesons are presented for p–Pb collisions at $\sqrt{s_{NN}} = 8.16$ TeV using the photon conversion method for the signal extraction. This method uses the tracking and particle identification capabilities of the central barrel detectors of ALICE. Signal extracted down to 0.3 GeV/c and 0.7 GeV/c for π^0 and η respectively. The resulting spectra are presented and systematic uncertainties have been evaluated. A suppression of the yield compared to pp collisions at the same center of mass energy is observed in R_{pA} for both mesons. Comparisons to theory predictions show consistency with the spectra and R_{pA}.

Declaration

I, the undersigned, hereby declare that the work contained in this research project is my original work, and that any work done by others or by myself previously has been acknowledged and referenced accordingly.

Signed by candidate

Samah Ahmed Mohamed AHMED, 15 December 2018

Acknowledgements

First of all, I would like to thank my supervisor Thomas Dietel for his support, continuous guidance and for giving me the opportunity to visit CERN and be part of the PCM group. I also thank and appreciate Friederike Bock, Lucia Leardini and all the PCM group for their help and support.

A very special thanks to Nicolas Schmidt, I am truly grateful and appreciate your dedication and helpful spirit since I started till I finished. I am very delighted that I worked with you, you made it more enjoyable.

Finally, Thank you to my family, friends, colleagues and my fiancé Musaab for supporting me always.

Contents

List of Figures

List of Tables

To my younger self, the journey was tough and very lonely. You grew up, learned a lot and became stronger....

Chapter 1

Introduction

The continuous pursue of human kind at all times is to unravel the mysteries of nature and answering questions like: where do we come from? and where are we going? The answers to such questions are the aim behind having all kinds of science and research. Researchers are studying how nature reacts to us and how we react to it, having experiments and recording observations to examine the behavior of things, starting from the molecule and reaching to far away galaxies. The physics community has witnessed a breakthrough by having the most powerful experiment ever built, the Large Hadron Collider (LHC). They succeeded to create a universe in the lab by accelerating particles and smash them together forming the exact phase of matter believed to have existed only microseconds after the big bang. This phase of matter formed when hadrons -the building blocks of matter- dissolve into their constituents, the quarks and gluons, and create a deconfined matter called the quark gloun plasma (QGP).

Investigating this strongly coupled medium is one of the purposes of the experiments at the LHC. Therefore, several observables that indicate the QGP production are studied. The first evidence is the suppression of high momentum particles and the energy loss in heavy ion collisions which is studied via the nuclear modification factor R_{AA}, which defined as the ratio of the measured yield in Pb-Pb collision to the yield measured in pp collisions scaled by the number of binary collisions.

As the energy loss is a signature of the hot nuclear matter effects i.e QGP existence. Further effects can occur like the cold nuclear matter effects due to the existence of a colliding nuclei.

The p-Pb collisions studied in this thesis play an essential role to distinguish the two nuclear matter effects. In contrast to what is expected from p-Pb collisions, LHC results show that a collective phenomenon is present which is an additional evidence of the QGP formation [2].
It is not certain yet if the collective behavior is evidence enough for the formation of a QGP in p-Pb collisions or it might be a resulting effect of different processes. All this makes the measurement of p-Pb collisions essential as it also serves as a baseline for Pb-Pb collisions as intermediate step between large and small systems. Furthermore, it provides an important reference to study QCD properties like the partonic structure of matter [3]. In particular, measuring neutral mesons spectra precisely is a base to extract direct photon yields from the large background of the decay photons. Direct photons are a powerful probe to study the QGP as they can carry information about all stages of the collision due to the fact that they can escape the medium unaffected [4]. Moreover, neutral mesons are a reference for jet quenching measurements in heavy ion collisions [5]

This thesis will present the measurements of neutral pion and eta mesons in p-Pb collisions at $\sqrt{s_{NN}} = 8.16$ TeV using the photon conversion method. The second chapter will give an overview of the current status of the theory behind the presented measurements. Afterwards, chapter 3 will discuss the detector system of the experiment as well as its performance. Chapter 4 is dedicated to the analysis of the collected data, going through all the steps required to extract the mesons. Finally, chapter 5 will present the results.

Chapter 2

Before QGP, QGP and after

A theoretical overview and basic concepts of particle physics will be presented in this chapter. Moreover, a brief theoretical background on the standard model, heavy ion collision and the Quark-Gluon Plasma will be discussed.

2.1 The Standard Model of Particle Physics

The Standard Model of Particle Physics succeeded in unifying three of the fundamental forces in nature: the electromagnetic, weak and strong nuclear forces. It describes the constituents and interactions of subatomic particles excluding gravity, by combining the quantum field theories of the electroweak interactions and quantum chromodynamics (QCD). QCD is the theory of the strong interaction between quarks and gluons.
The Standard Model classifies fundamental particles into two groups: Fermions and Bosons. Fermions are half spin particles that obey the Fermi-Dirac statistics and come as 6 quarks (up, down, charm, strange, bottom, and top) and 6 leptons (electron, muons, tauons, and their corresponding neutrinos).

Quarks have a color charge that has the same role as charge in electromagnetic interactions, however, colored particles have never been observed on their own due to the confinement property of QCD. Each particle has an anti particle with opposite charge and same mass.
Bosons are integer spin particles that obey the Bose-Einstein statistics. The strong interaction between Fermions are mediated by the gauge bosons which carry the color charge known as gluons, same as photons in the electromagnetic interactions. Therefore,

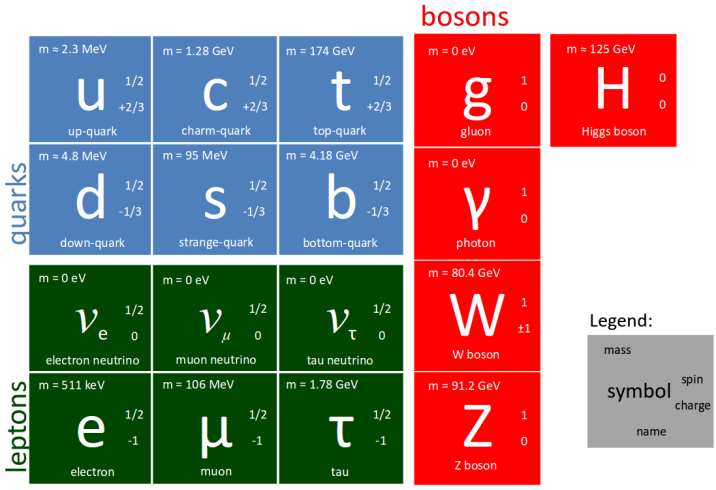

FIGURE 2.1: The fundamental particles of the standard model [6].

they also interact with each other. The weak force is mediated by heavy $W^{\pm}$ and Z bosons. Quarks and gluons are always in colorless states called hadrons.

Hadrons come in different categories: 3 quarks with different color charge (blue, green, red) called baryons, 3 anti-quarks with different anti charges called anti-baryons and one quark combined with anti-quark has color and anti color charge respectively known as mesons. Figure 2.1 is an overview of the standard model. The Lagrangian density of QCD is expressed as :

$$\mathcal{L} = \sum_q \bar{\psi}_a \gamma_\mu \left(i\partial^\mu - g_s A_q^\mu \frac{\lambda_a}{2} \right) \psi_q - \sum_q m_q \bar{\psi}_q \psi_q - \frac{1}{4} \sum_a F_a^{\mu\nu} F_{\mu\nu,a}, \tag{2.1}$$

where ψ_q represent the quark field, g_s is the effective strong charge, A_q^μ is a gluon field and λ_a are the Gell-Mann matrices. The term $F_a^{\mu\nu}$ represents the gluon field strength and can be written as:

$$F_a^{\mu\nu} = \partial^\mu A_a^\nu - \partial^\nu A_a^\mu + i g_s f_{abc} A_\mu^b A_\nu^c \tag{2.2}$$

QCD preserves the *chiral symmetry* for massless particles as they are invariant under the exchange of left- and right handed components of the quark spinor. The chiral symmetry is held as the quark is massless until, the strong force gives rise to a chiral condensate which leads to symmetry breaking. g_s expresses the strength of coupling quarks in QCD in terms of α_s as $\alpha_s = \frac{g_s^2}{4\pi}$

which is the running coupling constant of QCD. α_s depends on the momentum transfer Q^2, this dependence can be written in leading order by:

$$\alpha_s(Q^2) \approx \frac{12\pi}{(33-2N_f)ln\frac{Q^2}{\Lambda_a}}, \tag{2.3}$$

This equation can be used in pQCD only under the condition $Q^2 \gg \Lambda^2$, where Λ is the QCD scaling parameter that has experimental value $\approx$ 200 MeV. N_f is the number of quark flavors. The value of α_s is not predictable by QCD and can only be measured experimentally. Its value is much larger compared to the coupling constant in QED $\alpha_{em} \approx \frac{1}{137}$.
Additionally, another quantity to study for $q\bar{q}$ pair is the potential between them, it can be written as:

$$v_s = -\frac{4}{3}\frac{\alpha_s}{r} + Kr, \tag{2.4}$$

This equation interprets the confinement property of QCD which is the behavior at long distances (increase r) the potential grows linearly and consequently the energy. This makes liberating a quark from a hadron an impossible task as it would require an infinite amount of energy. That's why no single quark has been observed in nature. On the other hand for high momentum the coupling strength decreases and the particles become free particles, which is the second QCD property at short distances and high energies called as asymptotic freedom.
The last addition to the standard model of particles is the Higgs Boson which has zero spin and zero charge. The particle is an excitation of a component of the Higgs field that gives the fundamental particles of the standard model their masses. It was observed in 2012 by by the ATLAS [1] and the CMS [2] collaborations.

[1] A Toroidal LHC Apparatus (ATLAS)
[2] Compact Muon Solenoid experiment (CMS)

2.2 Quark Gluon Plasma in Heavy Ion Collisions

A new phase of matter that has an extreme condition of a very hot and dense perfect fluid of quarks and glouns is known as the Quark-Gluon Plasma. It is the same phase that believed to be existed 10 microseconds after the Big Bang. A collision of two heavy-ions at high energies can liberate the quarks and qluons creating this deconfined phase QGP.

We started colliding heavy ions 30 years ago using fixed tar-

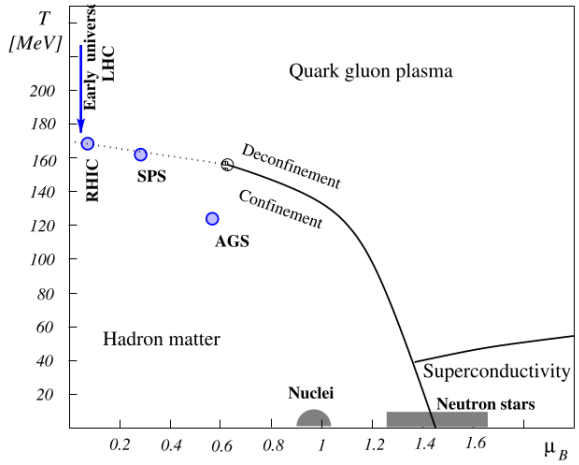

FIGURE 2.2: QCD phase diagram taken from [7]. At high temperature the figure shows a phase transition to a decnfined quark-gluon plasma also the chemical freeze out for RHIC, SPS and AGS are indicated.

gets in two experiments. They were first studied at the alternative Super Gradient Synchrotron (AGS) and the Super Proton Synchrotron (SPS) at CERN[3]. These experiments succeeded to get low center of mass energies of $\sqrt{s_{NN}}$= 4.6 and 17.2 GeV per colliding nucleon pair. To produce a medium with a very high baryon density considered as an intermediate phase which is mix between the hadron gas and the quark-gluon plasma as illustrated in figure 2.4[7].

The current center of mass energies achieved by the LHC[4] at CERN and RHIC at BNL[5] by accelerating the nuclei in opposite directions with speed very close to the speed of light in larger accelerator rings are dramatically large compared to what

[3]European Orgnaizaiton for Nuclear Research (CERN), Geneva, Switzerland
[4]The Large Hadron Collider (LHC)
[5]Brockhaven National Laboratory(BNL)

produced in the past. The two experiments operate with 5500 GeV and 200 GeV per nucleon pair in Pb–Pb and Au–Au collisions, respectively. In high energy colliders like LHC and RHIC a medium with a very low density (low μ_B) created at very large temperatures that liberate quarks gluon plasma [8].

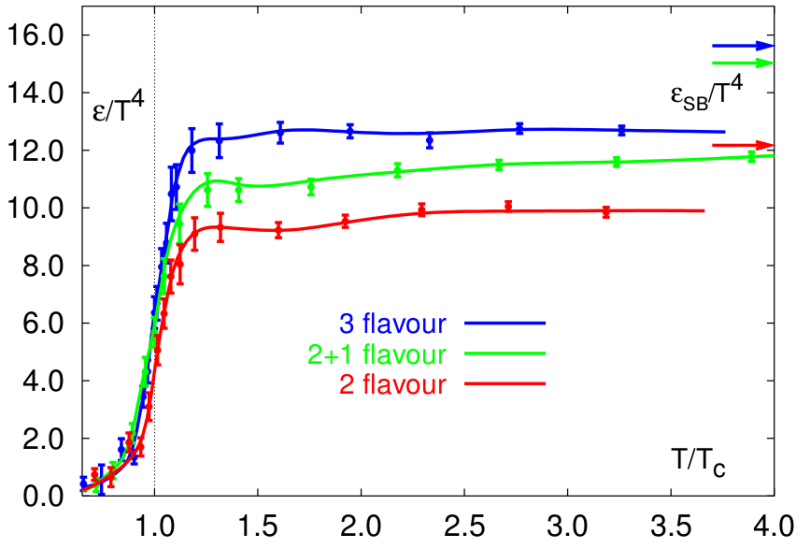

FIGURE 2.3: The energy density dramatically rises around the critical temperature. The flat line indicates no more degrees of freedom added to the medium. The arrows on the top right indicates the Stephan Boltzman limit where the system can be considered as an ideal gas [9]

The phase transition from hadronic matter to the deconfined phase increases the degrees of freedom in the system which occur at the critical temperature T_c. Depending on the considered quarks (QGP degrees of freedom) in lattice QCD (LQCD) calculations the critical temperature varies; leading to values of $T_c \approx 150 - 160$MeV at baryon chemical potential $\mu_B \approx 0$ [10]. A lattice calculation for the energy density divided by T^4 for different quarks compositions versus the critical temperature T_c is shown in figure 2.3.

Studying the signatures of QGP requires studying and understanding properties of the two ions collision which depend on the impact parameter b; the impact parameter b which is the

distance between the center of the colliding nuclei perpendicular to the beam axis. For the most central collisions the distance between the nuclei is too small and hence the impact parameter, illustrated in figure 2.4 the nucleons in blue involved in the collision called as participant and nucleons in gray not involved are called spectators.

The smaller the impact parameter the more central the collision and the larger number of participants. However, the impact parameter is not a measurable quantity. The centrality of a collision can be estimated from the number of participating nucleons N_{part}, binary nucleon-nucleon collisions N_{coll} i.e spectators $N_{spec} = 2A - N_{part}$ (A is the mass the number of the initial nuclei). Comparing these results to the Glauber model allows to get the impact parameter.

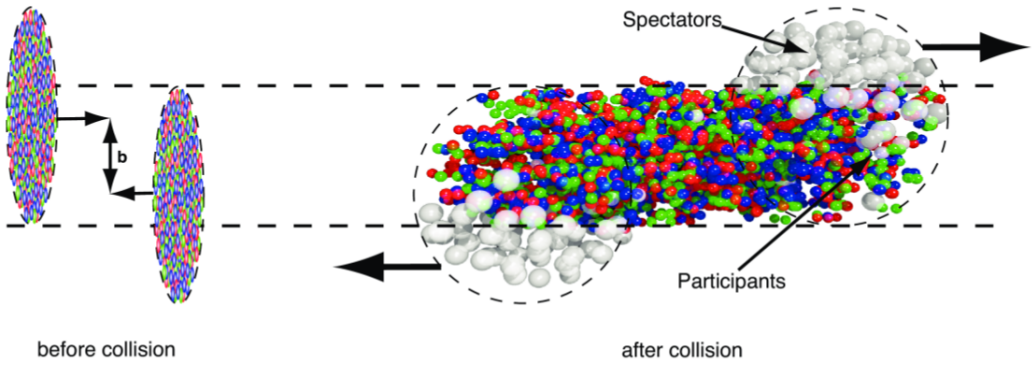

FIGURE 2.4: On the left: before the collision the two nuclei are Lorentz contracted. On the right after the collision the quarks and gluon are liberated [11]

In the case of p-Pb collision the collision system is much smaller. How the quark-gluon plasma evolves with time after the collision, how energy is distributed in the system and consequently how the properties of the medium change, will be discussed in the next section.

2.2.1 Evolution of the Quark Gloun Plasma

After the collision, the system undergoes a thermal equilibrium process. This process takes a thermalization time τ_o during which the energy is distributed in the overlap region, some models that explain the thermalization process can be found in [12, 13]. The standard scenario we will encounter here to explain the evolution after the thermalization is the Bjorken approach [14] where only the longitudinal expansion is assumed. The dynamics of the Quark Gluon Plasma (considered as perfect fluid) are determined by the local energy density ϵ and the local pressure P.

As the system expands the energy density reduces this leads the quarks and gluons to freeze out to hadrons again after the temperature becomes smaller than T_c. Before this state, the system will undergo an intermediate mixed phase which contains free quarks and gluons together with hadrons. During this phase the temperature stays constant.

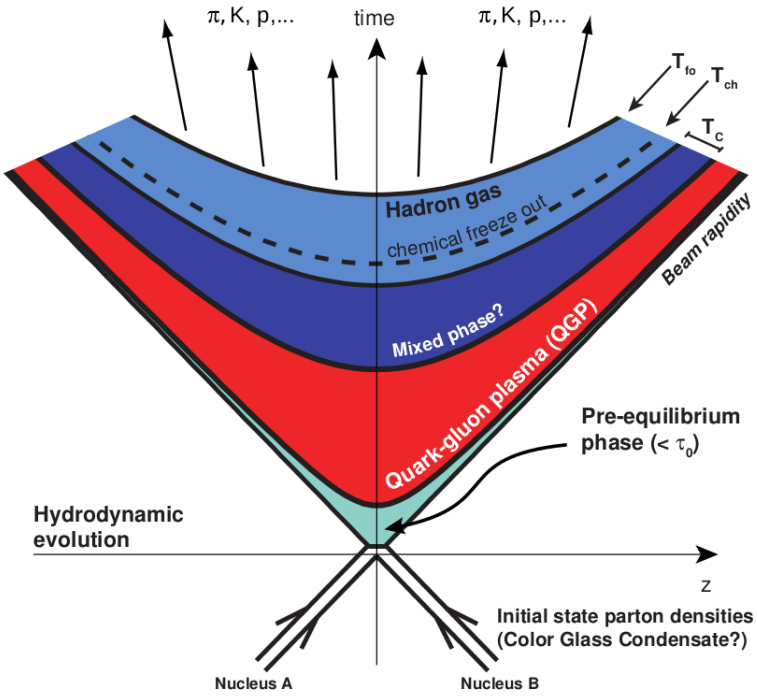

FIGURE 2.5: Space time evolution after the heavy ion collision. The system produces final state particles after it cools and freezes out. [15]

After the system freezes out below T_c a wide spectrum of particles is produced as shown in figure 2.5. Then, this spectrum can be changed by the inelastic hadron-hadron interactions until the system reaches the chemical freeze out temperature T_{ch} as indicated in the top right of figure 2.5. Afterwards, the system reaches a kinetic freeze out temperature T_{fo} at which all the momentum distribution of hadrons is fixed and all the elastic interactions stop [15]. Those particles are the detected material to investigate the quark-gluon plasma: do we observe the QGP? and what are the evidence of its existence?

2.3 Signatures of the QGP Phase Transition

The Quark Gloun Plasma has a very short lifetime of the order of 10^{-23} s which makes it very difficult to observe in the heavy ion collisions. There are several observables to help in investigating the existence of the QGP and which are considered as its signature. Some of these signatures are introduced here.

2.3.1 Particle Production in Heavy Ion Collisions

Taking a deeper look or a closer look into the properties of each heavy ion collision and the collisions by the hadrons and their constituents gives insights into the dynamical evolution of the bulk matter. The event properties are the multiplicity of charged particles N_{ch}, the yields of the identified and unidentified particles produced (transformed) as consequence of the energy loss in the collisions with mass m_0 and transverse momentum p_{T}.

The average multiplicity for the charged particles is the first observable that can be measured after the first collision as it doesn't need too much statistics. In the LHC all the experiments ALICE[6], ATLAS and CMS measured the charged particle density defined as the average multiplicity per unit of rapidity or pseudo rapidity y or η $\frac{dN_ch}{d\eta}$, which depends on the center of mass energy for pp and AA collisions as shown in figure 2.6.

[6] A Large Ion Collider Experiment (ALICE)

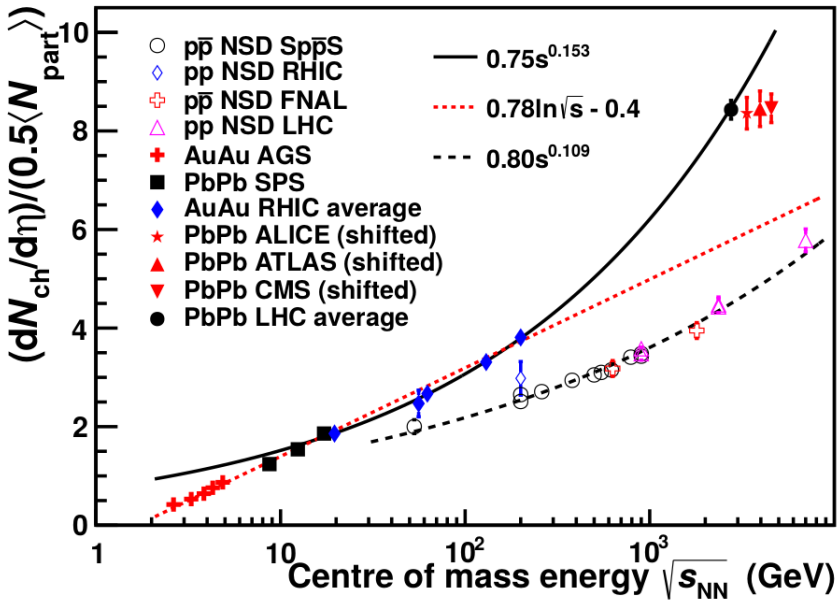

FIGURE 2.6: Charged particle pseudo-rapidity density, $\frac{dN_{ch}}{d\eta}$ per participant pair versus center of mass energy for pp and heavy ion collisions.[16]

$$\epsilon_{Bj} = \frac{< E >}{V} = \frac{< m_t >}{A_{t_o}} . \frac{dN}{dy} = \frac{1}{A_{\tau_o}} \frac{dE_T}{dy} \tag{2.5}$$

The measured charged particle density $(y \quad or \quad \eta)$ $\frac{dN_{ch}}{d\eta}$ by the LHC was found to be ≈ 1600 in the 5% most central events. Using the Bjorken's density by relating it to the energy density ϵ at the thermalization time $\tau_o = 1\text{fm/c}$ by the above formula [14].

2.3.2 Collective Flow

The QGP has an ordered motion when the mean free path of the particles is small, the pressure gradient leads to a collective flow. The flow reflects a strong correlation between the position of the particle and it is transverse momentum[16]. It depends on the initial conditions of the collisions. Therefore, it can be called *radial flow* in terms of the uniform azimuthal angle φ with respect to the reaction plane. More detailed information can be found in [17].

2.3.3 Anisotropic Flow

The formed overlap region after the collision of two nuclei has an almond shape varying as the impact parameter changes which expands in the x y plane as a result of the anisotropic pressure gradient being stronger in the shorter axis which is the reaction plane and Ψ_{RP}. The particle spectra are described with Fourier expansion [18],

$$E\frac{d^{3N}}{d^{3p}} = \frac{d^2N}{2\pi p_T dp_T dy}\dot{(}1 + 2\sigma_{n=1}^{\infty}\nu_n \cos[n(\varphi - \Psi_n)]), \tag{2.6}$$

where E is the energy of the particle, p_T is the traverse momentum, y is the rapidity, φ the azimuthal angle of the particle and Ψ_n is the angle in respect to the maximum anisotropy for the n^{th} order of the Fourier series and interpreted as the azimuthal orientation of the creation plane[18] and ν_n is the order of the contributing flow. The Fourier coefficients are p_T, y and are centrality dependent using the equation below,

$$\nu_n(p_T) =< \cos[n(\varphi - \Psi_n)] > . \tag{2.7}$$

For the most central collisions, higher harmonic are less dependent on centrality as the elliptic shape of the overlap region approaches a spherical shape. But, higher order harmonics are caused by the initial functions in the distribution of the nucleons [19]. For lower orders for ν_n like the second harmonic ν_2 is called the "elliptic flow" found mainly in non-central heavy ion collision resulting from the almond shape of the interaction region. While the first harmonic ν_1 is known as the directed flow which provides the deflection from beam direction at the two nuclei after the collision [11] higher order harmonics $\nu_{n's}$ help in understanding the evolution of the plasma and give estimates on some properties of the medium like the shear viscosity $\frac{\eta}{s}$. The collective flow of the medium could be thought of as a wave depending on the mass of particle with less flow for heavier particles at certain values for p_T. Thus heavier particles will have higher momenta [20].

2.3.4 Nuclear Modification Factor R_{AA}

After the creation of the QGP, a suppression of particle yield occurs due to the interaction with the medium. The quantity which expresses the modification of the spectra of a given observable such as p_T is called the nuclear modification factor which is calculated by the following equation

$$R_{AA} = \frac{\frac{d^2NAA}{dp_T dy}}{< T_{AA} > \frac{d^2\sigma_{pp}}{dp_T dy}}, \tag{2.8}$$

In words R_{AA} is the particle spectrum measured in heavy ion collisions divided by the scaled cross-section of the same particle in pp collisions. The quantity $< T_{AA} >$ which is the nuclear thickness function can be related to the Glauber model for a given impact parameter b.
R_{AA} will be equal to unity in case no interaction with the medium at $p_T >= 2$ GeV/c. This case is interpreted as a superposition of many binary collisions of the nucleons in heavy ion collisions. The mean number of binary nucleon-nucleon collisions N_{coll} can be calculated from the Glauber model for a given value of the impact parameter b, using the nuclear overlap function $< T_{AA} >$ and the inelastic cross-section of nucleon-nucleon collisions σ_{NN}^{inel} related by the equation:

$$< N_{ncoll} >_b = < T_{AA_b} > \sigma_{NN}^{inel}. \tag{2.9}$$

2.3.5 Cold Nuclear Matter Effects

This binary scaling will not be held in all states of the medium due to cold nuclear matter effect which occur in both collisions p-A and A-A. The p-Pb collisions are chosen to probe these effects as the formation of QGP i.e hot nuclear matter effect was not priori expected. The first effect is due to the structure of the nuclei that protons are not alone but bound to neutrons. Protons have a different quark substructure and different spin accordingly. Further bound nucleons are expected to interact differently from free ones thus, the parton density distribution is strongly modified [21]. The parton distribution function of

heavy nuclei related to the bound proton via the following expression

$$f_i^A(x,Q^2) = R_i(A,x,Q^2) f_i^p(x,Q^2) \tag{2.10}$$

Where R_i is the nuclear modification with respect to the free proton parton distribution function f_i^p depending on the fraction x that express the momentum of the nucleon carried by the parton, the momentum Q^2 and the mass number of the nucleus A. A schematic illustration of $R_i(A,x,Q^2)$ in different regions of nuclear modification in figure 2.7.

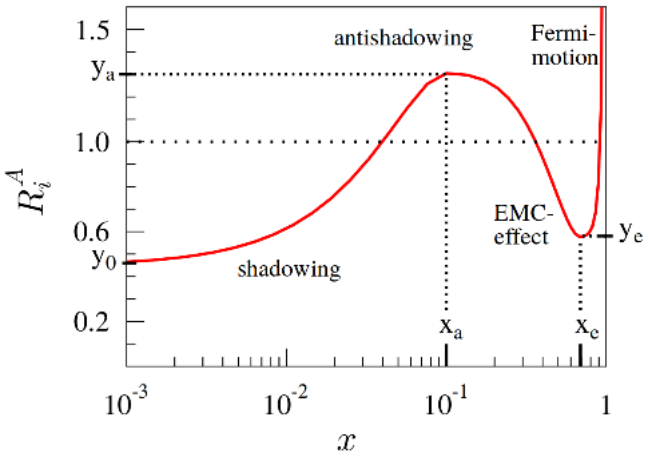

FIGURE 2.7: Schematic illustration how the nuclear modification$R_i^A(x,Q^2)$ varies with the momentum fraction x. [22]

For high momentum the function $R_i(A,x,Q^2)$ is greater than unity this is due to the increasing of particle production compared to the reference pp. The production increases due to the fact that nucleons are not still inside the nucleus what is so called "Fermi motion". While for low momentum the function is smaller than unity unlike what is expected, this suppression is not fully understood yet. Second initial effects are gluon saturation and nuclear shadowing of the parton density distribution in nuclei with respect to partons in the free nucleon which is responsible for the decrease of the parton momentum fraction $R_i(A,x,Q^2)$ again [21] shown in 2.7. All these initial effects have a role in varying R_{AA} and R_{pA}. [23], [24].
Additional effects can break the binary scaling such as the Cronin effect that is defined as the modification of the nuclear parton

density function PDFs with respect to nucleon PDFs. For instance, the multiple scattering of partons in a proton- nucleon collision causes an increase in the transverse momentum p_T which increases the transverse momentum p_T of the produced hadrons and results in an increase of R_{pA} as well[25]. Another effect that plays an important role in p-Pb collisions is the Color Glass Condensate (CGC). It is a theory that describes the gluon content of hadrons and nuclei in high energy collisions [26]. At low energies, the interactions of the nucleons constituents are considered. Whereas at high energies the nucleons are Lorentz contracted and the time dilation of their interactions leads to consider the constituents as free during the collision. The constituents are valence quarks as the color source at large x and luons at low x. Therefore, the gluon densities will increase until they reach a saturation level where the pQCD can no longer be applied but approximated by the CGC.
After the medium is formed, partons that traverse the strongly interacting quark-gluon plasma will lose energy due to interaction with partons in the medium in two ways: the first one is radiation which represents gluon Bremsstrahlung that occurs at high p_T. The second is multiple scattering known as collisional energy loss which occurs at low energies [27]. In both cases, the energy loss is negatively proportional to the parton energy which leads to a decrease of the average momentum of the produced hadrons and hence decreases the yield at high p_T with respect to pp collisions.

2.4 Photon Production in Heavy Ion Collisions

There are two mechanisms of particle production, according to the momentum transfer Q^2 dependent on the QCD coupling. When the momentum transfer Q^2 is large the coupling is weak, known as the hard process that can be described by perturbative QCD. The opposite case is the soft process which can be described by non-perturbative QCD.
Further discussion about the photon production in hadronic collisions will be introduced in this section.

Photons are an important probe for the quark-gluon plasma as they interact only electromagnetically. Therefore, escape the medium unaffected carrying information about the conditions of their production. This allows a better understanding of the quark-gluon plasma [28].
Photons produced in a nucleon-nucleon collision are called prompt photons. They are divided into two parts: direct photons and fragmentation photons. Additionally, there is a third type decay photon produced in processes like $q + g \longrightarrow q + \gamma$, $\bar{q} + q \longrightarrow g + \gamma$. About the nucleus-nucleus collisions, there are extra sources of photons added by the medium. The first source is the jet photon conversion and Bremsstrahlung photons. They are produced too early during the QGP phase when the temperature is the largest. As a production of the interaction between the jet and the hot medium by QCD Compton scattering.
The second source is thermal photons which have emitted from the thermally equilibrated QGP phase and form the hot hadron phase after the QGP. These photons give information about the thermodynamic state of the medium as the distribution of the transverse momentum depends on the temperature at which the photon was emitted.
However, jet photons and low momentum thermal photons have a special attention because they give insight into the temperature of the plasma. Direct photons spectrum is obtained by subtracting the background from meson with the double ratio method [29]. The subtracted meson decay photon spectrum γ_{decay} is mainly originally from π^0 ($\approx 80\%$) and η decays$\approx 18\%$, from the inclusive photon spectrum γ_{inc}. The direct photon signal extracted using the following equation:

$$\gamma_{direct} = \gamma_{inc} - \gamma_{decay} = \left(1 - \frac{\gamma_{decay}}{\gamma_{inc}}\right) \times \gamma_{inc}, \tag{2.11}$$

The ratio $\frac{\gamma_{decay}}{\gamma_{inc}}$ is calculated by equation 2.12 to reduce systematic uncertainty:

$$\frac{\gamma_{inc}}{\gamma_{decay}} = \frac{\gamma_{inc}/\pi^0}{\gamma_{decay}/\pi^0_{param}}. \tag{2.12}$$

2.4.1 Interaction of Photons with Matter

As mentioned before photons only interact electromagnetically although they do not have neither charge nor mass and have velocity equal speed of light. Therefore, they have the ability to travel for some distance before being involved in any interaction. Photons lose their energy partially or totally as they penetrates matter, this energy is transferred to an electron. Furthermore, photons interact via three mechanisms; the photoelectric effect, the Compton scattering and pair production.
In the following, only the pair production mechanism will be presented.

Pair Production This process can be described as when a photon penetrates the electromagnetic field of a nucleus an electron-positron pair is created for the energy of this photon, what is the so-called pair production.
As in any physical process, the energy and momentum are conserved what cause the angle of the conversions to be small for high momenta photons. Moreover, an expression for the differential cross section which is valid for high energies can be introduced in the equation below:

$$\frac{d\sigma}{dx} = \frac{A}{x_0 N_A}\left[1 - \frac{4}{3}x(1-x)\right] \tag{2.13}$$

Where A is the atomic number of the material, N_A is Avogadro's number and x_0 the total radiation length. Furthermore, the fraction of energy transferred to the pair produced is presented as $x = \frac{E}{K}$ where K is the total energy of the interacting photon. Taking this into account the cross section has to be symmetric between x and $1 - x$.
The total electron-positron pair production cross section at high energy is given by:

$$\sigma_{pair} = \frac{7}{9}\frac{AN_A}{x_0} \tag{2.14}$$

Where x_0 is the radiation length that is defined as the mean distance that over which a high energy photon loses about $\frac{1}{e}$ of its

energy via Bremsstrahlung and $\frac{7}{9}$ of the mean free path of pair production by a high energy photon [28].
Finally, the probability by which a photon converts after interacting with the material of thickness x in high momentum is given by

$$P_{conv} = 1 - exp\left(-\frac{7}{9}\frac{x}{x_0}\right). \tag{2.15}$$

Chapter 3

Experimental Setup

3.1 The Large Hadron Collider-LHC

The Large Hadron Collider (LHC) at CERN is] designed to collide protons and ions in a tunnel with a circumference of 27 km after accelerating them in several stages. Protons collide in a center of mass energy of ≈ 14 TeV/c and a luminosity of $10^{34}\text{cm}^{-2}\text{s}^{-1}$, whereas heavy ions like Lead ions are collided with 2 8 $TeVc$ per nucleon pair and a luminosity of $10^{27}\text{cm}^{-2}\text{s}^{-1}$. All these capabilities of the LHC make it the world's largest and most powerful hadron accelerator.
The stages that particles undergo to be pre-accelerated within the CERN accelerator complex shown in figure 3.1. The first steps to accelerate protons occur in the linear accelerator LINAC2 and BOOSTER, while heavy ions are accelerated in LINAC3. The following steps for both protons and Lead ions are Proton Synchrotron (PS) and the Super Proton Synchrotron (SPS). Hadrons circulate inside the LHC as bunches in tow beam pipes one. The two beam pipes are integrated into one pipe in the interaction regions. In order to maintain the hadron beam in a proper trajectory a magnetic field of 8.3 T needs to be produced by using superconducting magnets which are operated with liquid helium at 1.9 K. The collisions occur at the interaction points where the beam pipes cross. Then, the collisions are recorded by the four LHC experiments: ATLAS, CMS, LHCb, and ALICE. Each one of the experiments has a different goal and studies different properties of the collisions and hence a different kind of physics. For instance, ATLAS and CMS are general purpose

detector systems at the LHC. They aim to study particles originating from the primary vertex in the collision and they succeeded in discovering the Higgs Boson in 2012[30] [31]. Furthermore, both experiments investigate signatures of QGP[32] [33]. The LHC beauty experiment (LHCb) is also used to study CP violation in addition to investigating hadron decays to charm or bottom quarks, CP violation and super symmetry. The following section will explain the ALICE experiment in detail as it the only experiment that is fully dedicated to study the Quark-Gluon plasma (QGP) produced in heavy ion collisions.

Different collision systems recored by ALICE experiment such as pp,Pb-Pb and p-Pb collisions at different center of mass energies starting from $\sqrt{s_{NN}} = 2.76$ TeV till $\sqrt{s_{NN}} = 8.0$ TeV for p-Pb collisions at which the data sample analyzed in this thesis were taken in 2016.

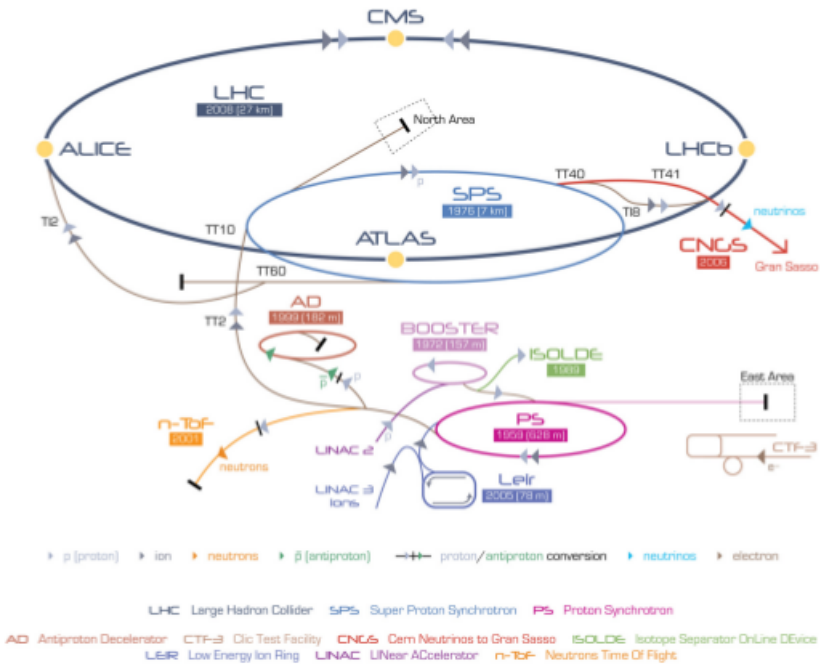

FIGURE 3.1: The design layout of the CERN accelerators complex.[1]

Detector	η acceptance	ϕ acceptance	position	main purpose
ITS				
SPD 1(2)	$\pm 2(\pm 1.4)$	full	$r = 3.9(7.6)$cm	tracking, vertex
SDD	± 0.9	full	$r = 15.0(23.9)$cm	tracking, PID
SDD	± 1	full	$r = 38(43)$cm	tracking, PID
TPC	± 0.9	full	$85 < r/\text{cm} < 247$	tracking, PID
TRD	± 0.8	full	$290 < r/\text{cm} < 368$	tracking, $e^{\pm}$ id
TOF	± 0.9	full	$370 < r/\text{cm} < 399$	PID
PHOS	± 0.12	$220^\circ < \phi < 320^\circ$	$460 < r/\text{cm} < 478$	photons
EMCal	± 0.7	$80^\circ < \phi < 187^\circ$	$430 < r/\text{cm} < 455$	photons and jets
HMPID	± 0.6	$1.2^\circ < \phi < 58.8^\circ$	$r = 490$cm	PID

TABLE 3.1: The coverage and purpose of the ALICE detectors[34]

3.2 A Large Ion Collider Experiment-ALICE

A Large Ion Collider Experiment (ALICE) is devoted heavy ion collision measurements [35]. Its purpose is to study the evolution of the quark-gluon plasma, therefore, a high momentum resolution at low transverse momentum is required as well as the ability to handle high multiplicities and still deliver good particle identification (PID). Figure 3.2 illustrates the ALICE detector and its all subsystems. The ALICE detector provides a magnetic field of 0.5 T aligned with the beam pipe by the embedded solenoid magnet shown in red in figure 3.2. The detector systems responsible for tracking, vertex finding, and particle identification are called the central barrel. The order of the detector systems starting from the closest to the beam pipe is the Inner Tracking System (ITS), then comes the Time Projection Chamber (TPC), the Transition Radiation Detector (TRD), followed by the Time Of Flight (TOF), the High Momentum Particle Identification (HMPID) and two calorimeters are known as the photon Spectrometer (PHOS) and the Electromagnetic Calorimeter (EMCal). The main purpose of the central barrel detector systems, the coverage, and the position is shown in the table3.1
The next section will discuss the different central barrel detector systems shown in figure 3.2.

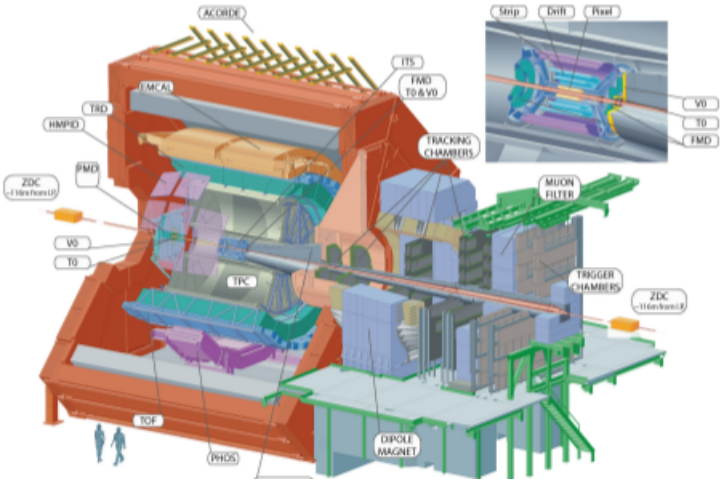

FIGURE 3.2: The ALICE detector with all the sub detectors[36]

V0 Detector (V0)

The $V0$ detector is composed of two scintillator arrays,VOA VOC which located on both sides along the beam axis at z = 340 cm and z= 30 cm successively[35]. Both scintilator arrays covers pseudorapidity in the range $2.8 < \eta < 5.1$ for VOA and $-3.7 < \eta < -1.7$ for VOC. The $V0$ detector is used as a minimum bias trigger as well as providing information about the centrality in heavy ion collisions[37][38].

Inner Tracking System (ITS)

The ITS [34]is designed to reconstruct the primary vertex of the collision and secondary vertices from meson decay with a resolution not less than 100 μm. Therefore, the ITS is the closest detector to the beam pipe. ITS consists of six layers of silicon. The two innermost layers are known as the Silicon Pixel Detector (SPD). The high granularity of two SPD layers gives the ITS the ability to handle the largely charged multiplicities in heavy ion collisions of up to $\frac{dN_{ch}}{dy} \approx 1$. The ITS with its six layers of silicon detectors cover a pseudorapidity range in the laboratory system of $|\eta_{lab}| < 0.9$. The subsequent ITS layers are The Silicon Strip Detectors (SSD) and two Silicon Drift Detectors (SDD)[39]. ITS has the capability to identify particles with $p_T < 200\,\mathrm{MeV/c}$ in addition to reconstruct vertex precisely. Therefore, the momentum and angular resolution to reconstruct particles by the

TPC can be improved and particles that traverse dead regions of the TPC can still be reconstructed using the SDD and SSD via $\frac{dE}{dx}$ measurement in the non-relativistic region. This allows the ITS to identify particles with transverse momenta down to about 80 MeV/c. Furthermore, due to the good resolution of the ITS, it is able to remove the in-bunch pileup events that occur when there are many collisions lead to make the tracks coming from different vertices overlap and hence be not distinguishable in the detector.

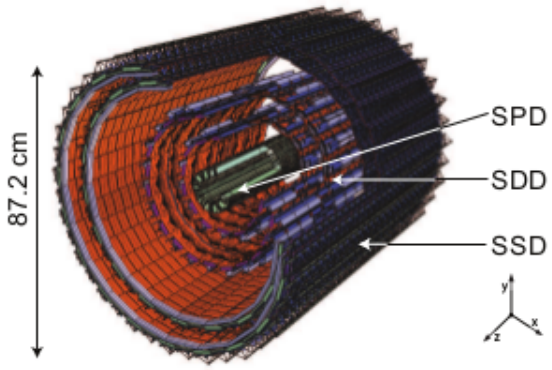

FIGURE 3.3: The inner tracking system with a detailed view and all sub-detectors.[40]

The Time Projection Chamber (TPC)

The TPC [41] surrounds the ITS and is the main detecting device of ALICE, considered as the central barrel detector of charged particles tracking and particle identification. It covers a pseudorapidity range of $|\eta_{lab}| < 0.9$ over a 2π azimuthal angle. The TPC is capable to handle high multiplicity heavy-ion events. It is designed as a cylindrical drift chamber with a gas volume of 90 m^3 and extends 2.5 m in beam direction on each side of the interaction point. Figure 3.4 shows a three-dimensional sketch of the TPC field cage.

The TPC active volume ranges from 85 cm to 250 cm in the radial direction with full length of 500 cm. It is filled with a drift gas which is aa mixture of 90% Ne and 10% CO_2 [6]. The gas volume is divided by central electrode at $\eta = 0$ and $z = 0$

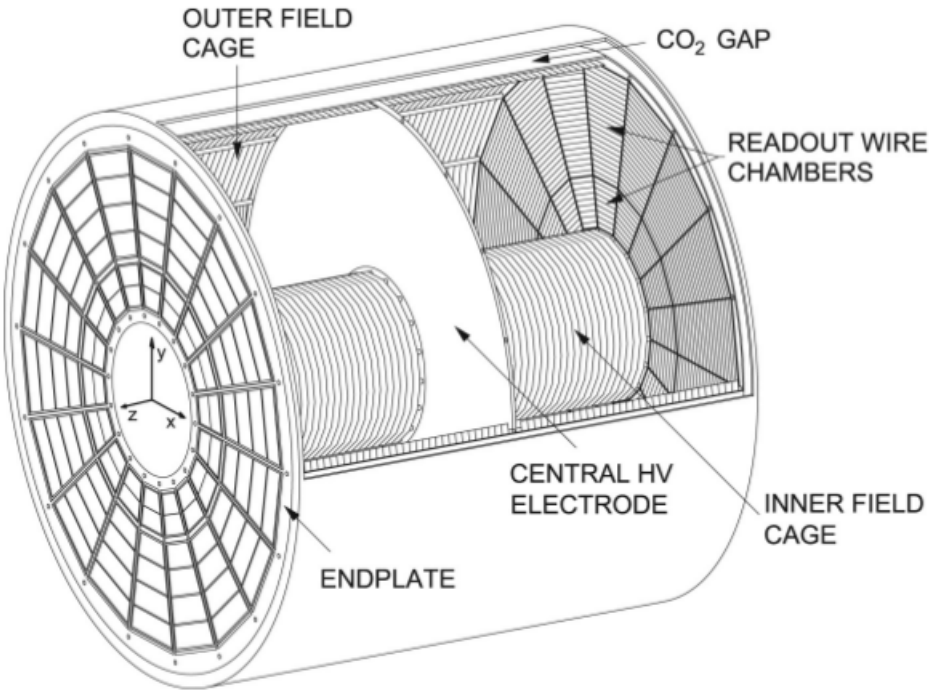

FIGURE 3.4: Sketch of the layout of the Time Projection Chamber.[41]

into tow symmetric drift volumes positioned at the axial center and aligned to the interaction point . A voltage of 100 kV is applied to the central electrode, in drift times of electrons from the ionization of the TPC gas mixture and an electric field of 400 V/cm is created towards the end plates. At the end of the plates there exists the high drift field is needed to keep the drift time of the TPC short readout pads which consist of multi-wire proportional chambers (MWPCs) with cathode readout and segmented into 18 sectors each covering 20° in azimuth with each composed of two chambers in the radial direction. In order to get an accurate three dimensional measurement of the trajectories of charged particles the TPC end plates to need to be equipped with 557568 readout channels to have a precise measurement of the arrival point of the electrons combined with an accurate measurement of the arrival time. The curvature of the tracks in the magnetic field of the $L3$ magnet is used to determine the charged particles momenta. Primary tracks with $100\,\mathrm{MeV/c} < p_\mathrm{T} < 100\,\mathrm{GeV/c}$ can be reconstructed in the TPC only if the particle traverses through at least one third of the TPC in the radial direction. However, secondary tracks can be

reconstructed down to 50 MeV/c.
In addition to the tracking capabilities, the TPC is also capable to identify particles with a resolution for the transverse momentum of about 1 GeV/c via measuring the energy loss in the drift gas. The energy loss per path length is described by the Bethe-Bloch-formula as shown in figure 3.5. The resolution in the ionization signal is 5%.

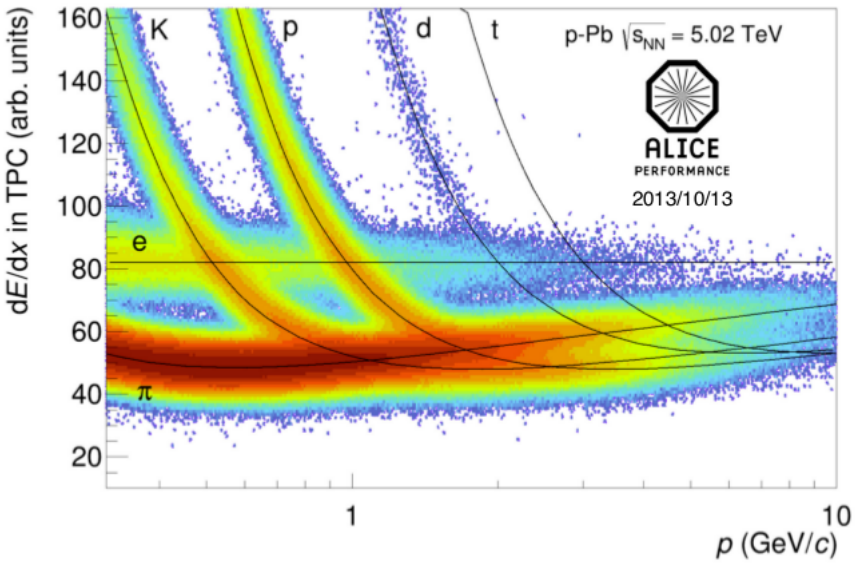

FIGURE 3.5: The energy loss by the particles in the TPC versus the momentum p_T. Black lines show BetheBloch parametrization.[42]

Electromagnetic Calorimeters-PHOS and EMCAL

For the presented neutral meson analysis the Calorimeters were not used but as they have been installed in the ALICE setup to observe the initial phase of heavy ion collisions as well as it's thermal and dynamical properties. The following pages will give a short explanation about the Photon Spectrometer PHOS and the Electromagnetic Calorimeter EMCAL.

PHOS

The Photon Spectrometer PHOS [43] is composed of a single-arm electromagnetic Lead tungstate ($PbWO_4$) calorimeter which

has a high granularity to measure energy and hit coordinates of particles. PHOS is positioned at a radial distance of 4.6 m from the interaction point of ALICE and covering pseudorapidity of $|\eta_{lab}| < 0.12$ and azimuth angle $260^\circ < \phi < 320^\circ$ and it consists of three detector modules with 3584 detection channels.
The reason behind choosing a Lead tungstate as a detector material is to fulfill the requirements imposed by the high multiplicity of central collisions as it has a small Moliere radius and high density. When measuring neutral mesons, π^0 and η via counting their decay photons a highest rapidity density of $dN/dy = 8000$ lead to almost 16000 clusters per rapidity interval. A high segmentation at the order of the Moliere radius as well as a large distance to the interaction point is required to resolve the overlapping showers hence, 2.2$\times$ 2.2 cm a transverse cell size was chosen.

EMCAL

The Electro Magnetic CALorimeter (EMCal) [35], [44] differs from PHOS as it has an inferior position and energy resolution with larger acceptance but it matches PHOS that it is positioned 4.5 m aware from the interaction point. It is designed to improve the capability of ALICE of jet measurements. Moreover, to measure single particles like π^0 or electron up to high p_{T}.
EMCal is a large Pb-scintillator calorimeter which has a longitudinal wavelength-shifting fiber light collection and a cylindrical geometry. In this way, it can fit in the free space between the ALICE space frame and the ALICE magnet coils inside the $L3$ magnet. It has two types of super-modules: the ten full-size modules which have a coverage of $\delta\eta = 0.7$ and $\delta\psi = 20^\circ$ whereas, the two smaller super-modules have half of the acceptance in ψ. The EMCal uses 12288 towers aligned to point to the interaction zone, each module composed of 2×2 towers and every module consists of 12 stripes of 24 modules but smaller modules have 6 stripes only. There is a gap with a width of 3 cm between the super-modules aligned with the TPC sectors boundaries. Otherwise, the amount of material on the TPC frame would degrade electromagnetic measurements in the gap regions.

3.3 Reconstruction

3.3.1 The ROOT and AliRoot Framework

The ALICE offline framework extension of ROOT is AliRoot which the framework used to analyze neutral meson data presented in this thesis [45]. It is built to deal with the massive amounts of data produced by the ALICE detector systems. Root is an object orientated framework implemented in C++ [46] and developed at CERN by Rene Burn and Fons Rademakers to replace the previous framework used which was written in FORTRAN. ROOT has more efficient tools to do particle physics analysis and to visualize physics processes using a graph, histograms, and other mathematical operations.
The AliRoot together with AliPhysics packages are used to process raw data and interface with event generators like PYTHIA [47], HIJING [48], DPMJET [49] and EPOS [50] to produce MonteCarlo (MC) simulations as well as data reconstruction. The above-mentioned generators can simulate the collision to produce all primary particles. GEANT [51] is responsible of simulating the detector response and the path of the particle through the detector and it's interaction with the detector material.

There are two formats to store the reconstructed events the first is Event Summary Data files (ESD) and the other is Analysis Object Data (AOD) files. ESD files contain all the reconstruction and track parameters and it is the same format used to store data analyzed in this thesis. whereas AOD files are compressed and only contain relevant information for the analysis.
The whole AliRoot is under continuous development to improve general performance, and it is connected to the computing grid used by ALICE collaboration via AliEn system [52] to deal with the tremendous amount of data produced by the LHC.
This analysis is to analysis neutral mesons via conversions using the analytical framework of the Photon Conversion Group PCM [53].

3.3.2 Charged Particle Tracking and Primary Vertex Reconstruction with ALICE

The event reconstruction in the central barrel of ALICE is the first step toward charged particles tracking. Event reconstruction is done by determining the primary vertex of the interaction before starting to reconstruct tracks, the primary vertex reconstruction is performed based on information taken from the SPD. A rough estimate of he preliminary primary vertex is made from the z coordinates of the two reconstructed pairs i.e tracklet required in two layers of the SPD. The following step is to optimize a final vertex by by repeating the same procedure moreover the x y coordinates can be determined precisely. The level of measurement accuracy is determined by the resolution in z which is expressed by:

$$\sigma_z = \frac{A}{\sqrt{dN_{ch}/d\eta}} + B \tag{3.1}$$

A = 290 μm and B is a few micro meters to consider the residual misalignment of the silicon pixel layers [40]. The resolution depends on the multiplicity and hence on charged particle density. There is a possibility to have more than one primary interaction in a single bunch crossing associated with additional primary vertices, called as same bunch pileup. The vertex algorithm must be repeated when the pileup is expected, usually, events with pileup are removed for the analyses. Eventually, the primary vertex is defined as the one with the highest number of contributing tracklets [54].
The step comes after reconstructing a primary vertex is to apply a full track finding procedure starts inside the TPC using the Kalman filter [55]. Two combined clusters are used as the seed for the tracks, a cluster can be defined as a set of several digitized detector signals in pad-row and time direction [15]. Another approach is to use three clusters without the vertex information as seeds propagated inwards. There is a certain criterion by which good tracks are determined, first, the track should have more than 20 clusters and at least 50% of all the detected clusters are

accepted. Therefore, the quality of the clusters is decided depending on the cluster density, the number of clusters and momentum. Tracks have poor quality are rejected. The TPC is capable of clearly separate and identify particles via the specific energy loss dE/dx by the particle. The ITS track finding process starts from the track propagation of the reconstructed TPC tracks to the outermost ITS layer taken as seeds. This process can be disturbed by several sources of noise like multiple scattering of that particle. At each ITS layer the seeds are updated if a cluster lies within a proximity cut then the updated seed is saved as a new seed. The TPC track outcomes in a tree of track hypotheses in the ITS. Some detection inefficiencies might cause missing clusters within the proximity cut, in order to deal with this inefficiencies the χ^2[1] of the seed used for tracking must be increased. Tracks reconstruction at low p_{T} for the ITS combined with TPC is very limited because particles at low p_{T} have tracks with a radius that is not sufficient to traverse $1/3$ the radial TPC length. Furthermore,the reconstruction at low p_{T} is restricted by the energy loss and multiple scattering in the detector material, the reconstruction achieved for the combined ITS-TPC tracks is down to 200 MeV/c for pions and 400 MeV/c for protons.
For clusters that were not used in ITS-TPC tracks a standalone ITS tracking is performed.Therefore, a helical seeds are chosen from two clusters of the three innermost ITS layers combined with the interaction vertex and propagated outwards. The Kalman filter is used to refit the track hypotheses and accept tracks with the best χ^2. Reconstruction of low p_{T} particles is improved down to about 80 MeV/c by using the ITS standalone tracking.Then, all tracks are extrapolated to their point of closest approach to the preliminary interaction vertex. Afterwards, the clusters from the previous step are used to refit the tracks with the Kalman filter what is so-called outwards propagation. Further outwards propagation is needed as the track reach the outer TPC wall to coincide with signals in the neighboring detectors e.g Time

[1] $\chi^2 = \sum_{i=1}^{s} \left(\frac{y^i_{measured} - y^i_{expected}}{\sigma_i} \right)^2$ where:$y^i_{measured}$ is measured p_{T}, $y^i_{expected}$is expectedp_{T}, s is the number of p_{T} bins and σ is the systematic uncertainty

Of Flight TOF, Transition Radiation Detector TRD or the electromagnetic calorimeters. Step by Step the track length integral and the time of flight of different species of particles are updated. However, detectors at radii larger than the TPC contribute with information that is stored to the track object and can be used for particle identification but they are not necessarily involved in updating the track kinematics.
The last reconstruction step is all the tracks are propagated inwards again and refitted in TPC and ITS hence, to determine the track's position, direction, inverse curvature, and the covariance matrix. Eventually, after the tracking is complete the global tracks are used to determine the final interaction vertex with high precision. The scheme of track, reconstruction is drawn in figure 3.6

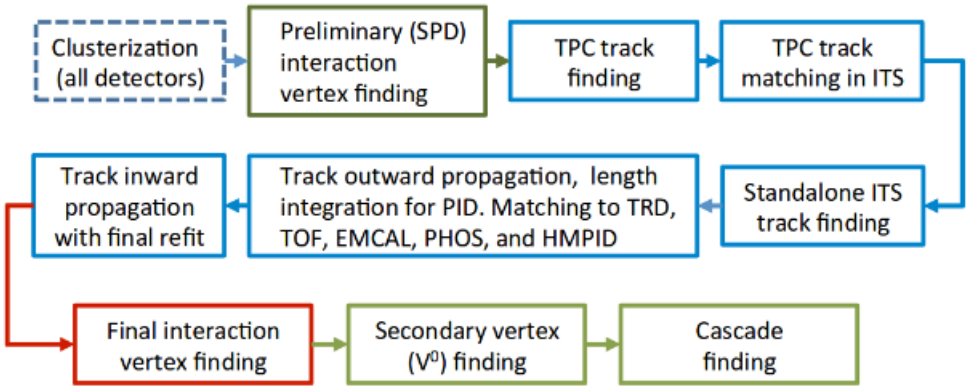

FIGURE 3.6: Event reconstruction flow in ALICE.[36]

Chapter 4

Neutral Meson Analysis using the Photon Conversion Method

The neutral mesons π^0 and η can be measured via their two-photon decay channel as they have a very short lifetime that makes it impossible to directly detect them. However, a method called Photon Conversion Method (PCM) succeeded in measuring neutral pions π^0 down to p_T of 0.3 GeV/c and 0.7 GeV/c for η. This chapter will introduce the neutral meson analysis in p-Pb collisions at $\sqrt{s_{NN}} = 8.16$ TeV in detail. First, we are presenting the measured datasets and the MontCarlo simulations as well as the event selection in section 4.1. Then, section 4.2 discuses the reconstruction and selection of conversion photons. Extracting the signal of neutral meson and corrections applied to the raw yield comes in section 4.4 and 4.3. Finally the systematic uncertainty is evaluated and presented in section 4.5.

4.1 Data Sets and Quality Assurance using MC Simulations

The data we study in this thesis is reconstructed after the p-Pb collision at 8 TeV by the ALICE detector. The data sets have two periods which have been recorded in 2016. The periods for collecting data were between 17 - 25 November and between 25 November - 4 December. Each period was divided into multiple runs. The photon reconstruction and electron identification quality are assured by checking the agreement between data and MC in certain quantities. The following sections will discuss these quantities in detail.

4.1.1 MonteCarlo Simulations

Two Mont Carlo event generators combined with a full detector simulation with Geant 4 have been used to do the correction to spectra of the data. The productions by DPMJET and EPOS were anchored to the data samples having the same detector conditions as the data periods. A brief explanation of the two generators DPMJET and EPOS follows in the next paragraphs.

DPMJET The DPMJET generator is based on the dual parton model [56]. This model deals with low momentum transfer and a large coupling constant α_s production of particles. Therefore, this model is based on the large-N expansion of non-perturbative QCD and the Reggeon field theory. Table 4.1 shows the statistics available for both data samples and MC productions for the minimum bias and different multiplicity bins.

EPOS [50] is a Monte Carlo generator based on The Parton-Based Gribov Regge Theory [57]. It is a new parton model approach based on effective QCD for hadron-hadron interactions in the initial states of the collision at extremely high energies. The model treats the soft interactions as well as the hard scattering. Furthermore, this model solves the deficiencies of other models dedicated to high energy physics like PYTHIA as it failed to reproduce particles with low momenta accurately.

4.1.2 Event Selection in pPb collision

Data taken from p-Pb collision at center of mass energy $\sqrt{s_{NN}}$= 8.16 TeV is used for minimum bias analysis. For this analysis, the default minimum bias trigger trigger requires two hits in the $V0$ detectors $V0A$ and $V0C$. All the events used to calibrate the detector were rejected as well as events that do not have primary reconstructed vertex Z with $|Z_{vtx}| < 10\,\text{cm}$. The fraction of events rejected due to missing primary vertex and the fraction of events rejected due to a vertex position outside 10 cm are shown in figure 4.1.

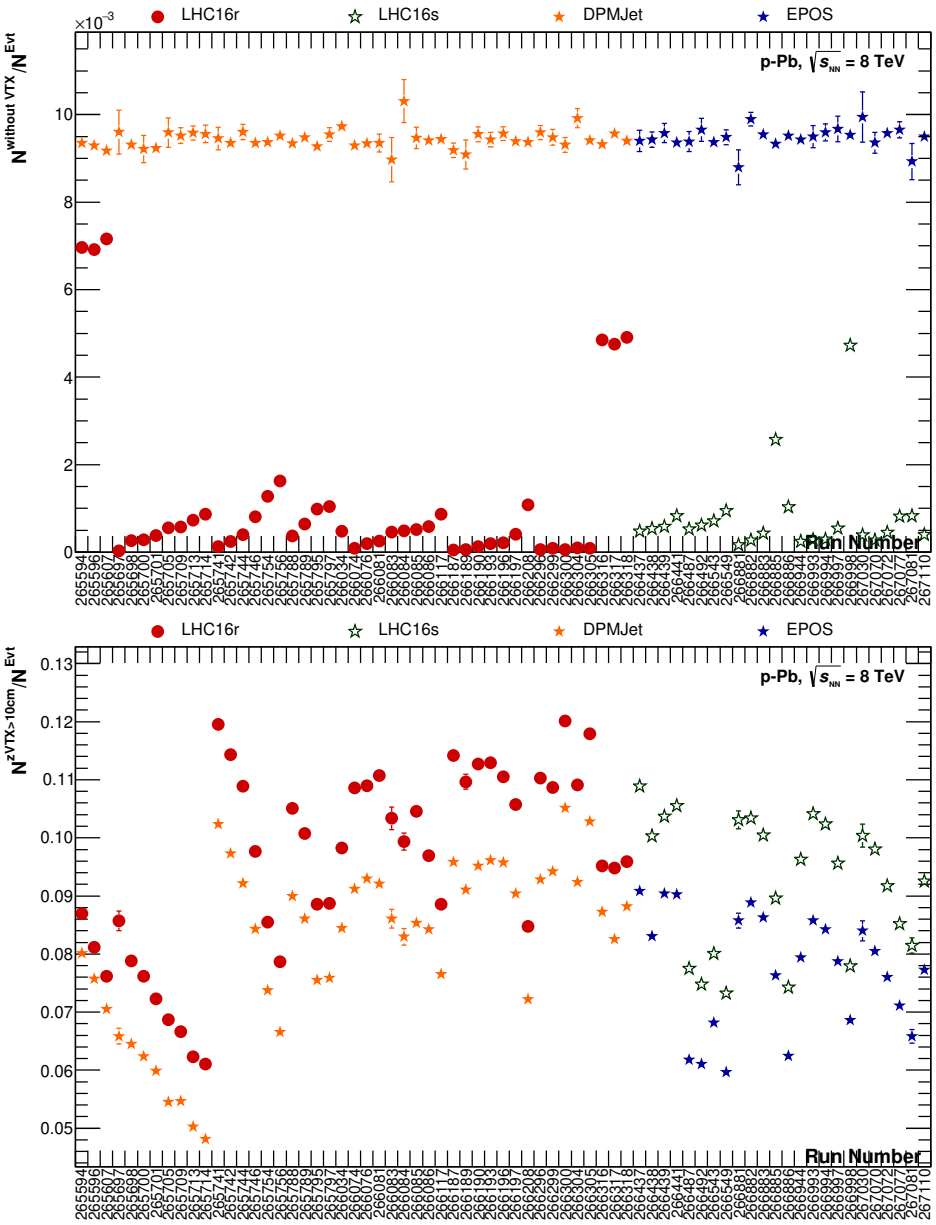

FIGURE 4.1: Top: Fraction of events rejected due to missing primary vertex with respect to the total number of collected minimum bias events in the respective run. Bottom: Fraction of events rejected due to a vertex position outside $Z_{vtx} = \pm 10$ cm with respect to the total number of collected minimum bias events in the respective run.

The total event summary data (ESD) available for the minimum bias is about 52 million events. In addition, another quantity has been analyzed as part of the quality assurance QA which is the mean number of tracks in the TPC and the fraction of photon candidates in p-Pb events normalized to the number of events illustrated in figure 4.3. The analyzed centralities in

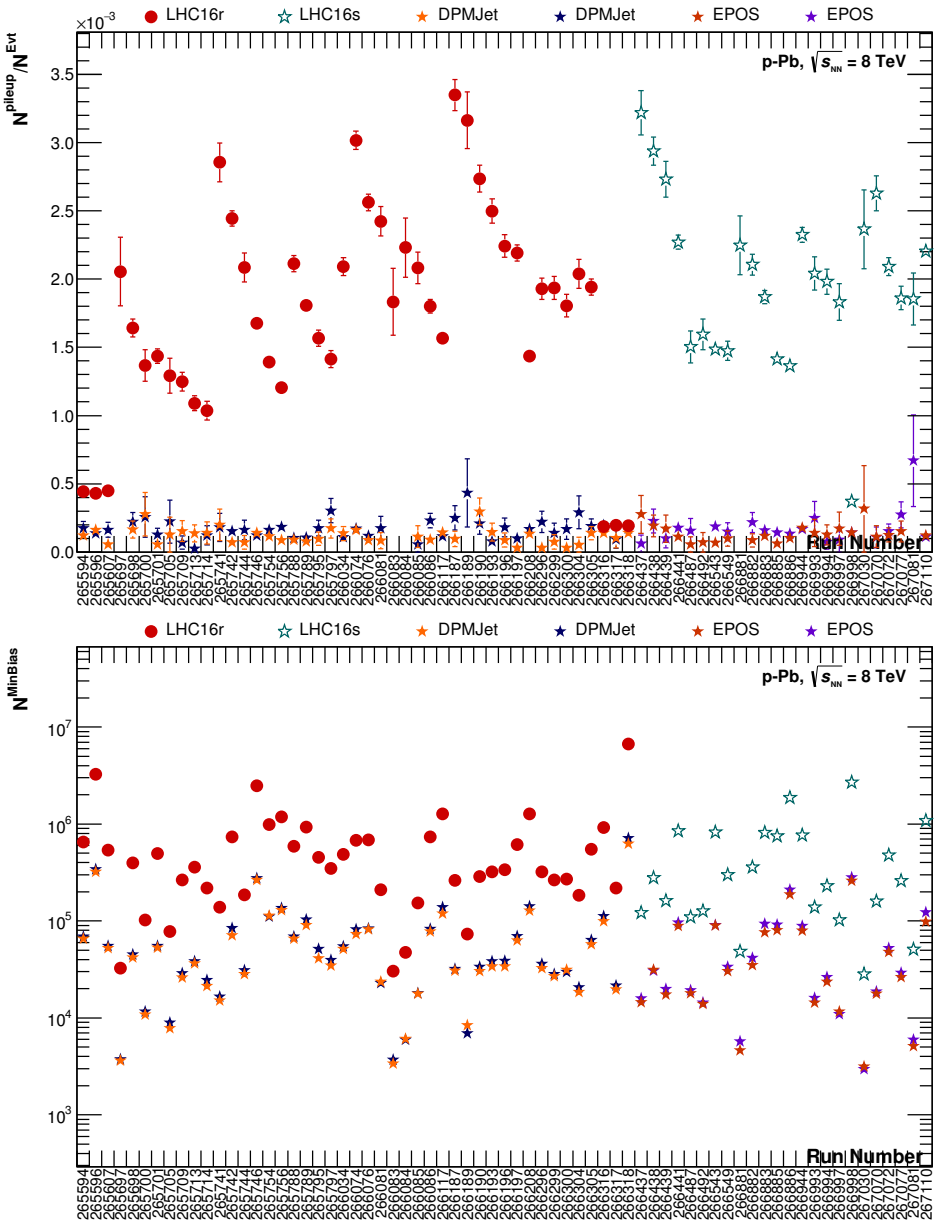

FIGURE 4.2: Top: Fraction of events rejected due to the SPD pileup condition with respect to the total number of collected minimum bias events in the respective run. Bottom: Number of minimum bias events per run.

this analysis beside the minimum bias are $0-20\%$, $20-40\%$, $40-60\%$, $60-100\%$; wider centrality bins chosen compared to bins chosen for Pb-Pb collisions due to much smaller statistics for p-Pb collisions.

The data taking rate in ALICE is limited by the Time Projection Chamber TPC, due to the long drift times for the electrons in the chamber. The fraction of pileup event normalized to the total minimum bias events and number of minimum bias events

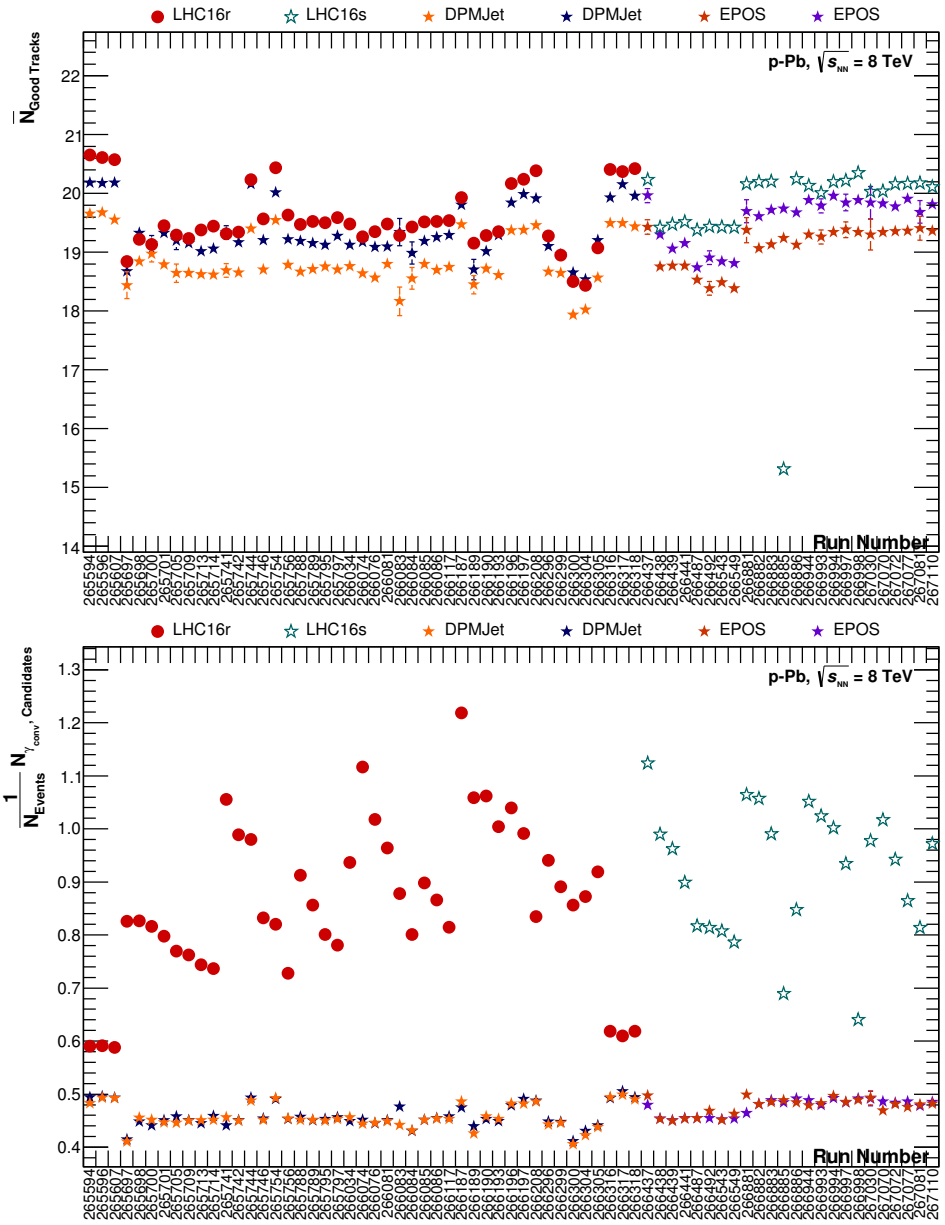

FIGURE 4.3: Top: Fraction of events rejected due to the SPD pileup condition with respect to the total number of collected minimum bias events in the respective run. Bottom: Number of minimum bias events per run.

are shown in figure 4.2. To prevent events from overlapping and creating pile-up, both beams at the ALICE interaction point were displaced to reduce the interaction rate. However, reducing the interaction rate still doe not guarantee only one event detected at a time. The pile-up can occur within the same bunch and called as 'in-bunch-pileup' and also occur 'out-of-bunch' pile-up. Those vertices are reconstructed using the Silicon Pixel

Detector (SPD) tracklets. The events that show SPD pileup rejected depending on the number of tracklets as the primary vertex with the highest number of tackles expected to have pileup. The higher the luminosity or the smaller the beam diamond the larger the fraction of rejected events.
Further, events that have more SPD clusters than SPD tracklets are considered as 'background event' and discarded from the analysis by applying the following cut:

$$N_{\text{Clusters}} > 4 \times N_{\text{Tracklets}} + 60 \tag{4.1}$$

	Sample	$\sqrt{s_{NN}}$	Multiplicity	Accepted Events
Data	LHC16r.pass1	8.16 TeV	min bias	31.131e+07
			0-20%	4.5106e+06
			20-40%	4.5246e+06
			40-60%	4.491e+06
			60-100%	8.6688e+06
	LHC16s.pass1	8.16 TeV	min bias	1.1803e+07
			0-20%	2.1263e+06
			20-40%	2.1335e+06
			40-60%	2.1312e+06
			60-100%	2.1144e+06
MC	LHC18f3b	8.16 TeV	min bias	3.9950e+07
			0-20%	7.379e+06
			20-40%	8.859e+06
			40-60%	8.029e+06
			60-100%	1.568e+07
	LHC18f3c	8.16 TeV	min bias	1.325e+07
			0-20%	2.4838e+06
			20-40%	2.961e+06
			40-60%	2.728e+06
			60-100%	5.0730e+06

TABLE 4.1: Number of events passing our event selection in p-Pb for data and Monte Carlo simulations.

4.2 Photon reconstruction and selection

The photons convert into two daughter tracks forming a V like shape. One track is for e^- and the other for e^+. Those two tracks

are reconstructed with a secondary vertex referred to as V^0 [36]. The V^0 finder helps to find all secondary tracks that are oppositely charged and have the distance of closest approach (DCA) up to 0.5 mm from the primary vertex. Figure 4.4 illustrate the V^o finder principle.
When reconstructing massive particles, an assumption is made that the opening angle between the two oppositely charged tracks is not zero to optimize the V^o finder. Moreover, the opening angle for the conversion of a massless photon is close to zero, therefore, the calculated conversion point might be displaced. Thus, another assumption is made to improve the resolution of the conversion point. The secondary vertex is recalculated under the assumption that the momenta of the conversion products are parallel at the point of their creation. More details about the mean resolution of the conversion point determined by PCM can be found in [58]. It is better than $3\mu rad$ in ψ, while the resolutions R and Z are approximately 1.3 cm and 0.8 cm respectively [28].

Photons are not the only reconstructed V^0 sample, they are together with K^0_s, Λ, $\bar{\Lambda}$. Therefore, several selection criteria need to be applied in order to select photons only. There are three categories of cuts: the track and V^0 selection to ensure a good track quality, particle identification cuts for electron selection and pion rejection and the photon selection cuts. The following subsection will discuss them in more detail.

4.2.1 Track and V^0 selection

The track and V^o cuts is the first category that reflects the basic track and V^o selection criteria. Table 4.2 shows the standard cuts for the analysis in terms of this category.

For this analysis, the standard V^o -finder type is the On-the-Fly V^o finder which runs during the initial reconstruction of the tracks while the offline V^o -finder runs after processing the tracks and are used for crosschecks and in the material budget uncertainty i.e. the error that is due to the lack of material in the detector which needed to interact with photons and due to the

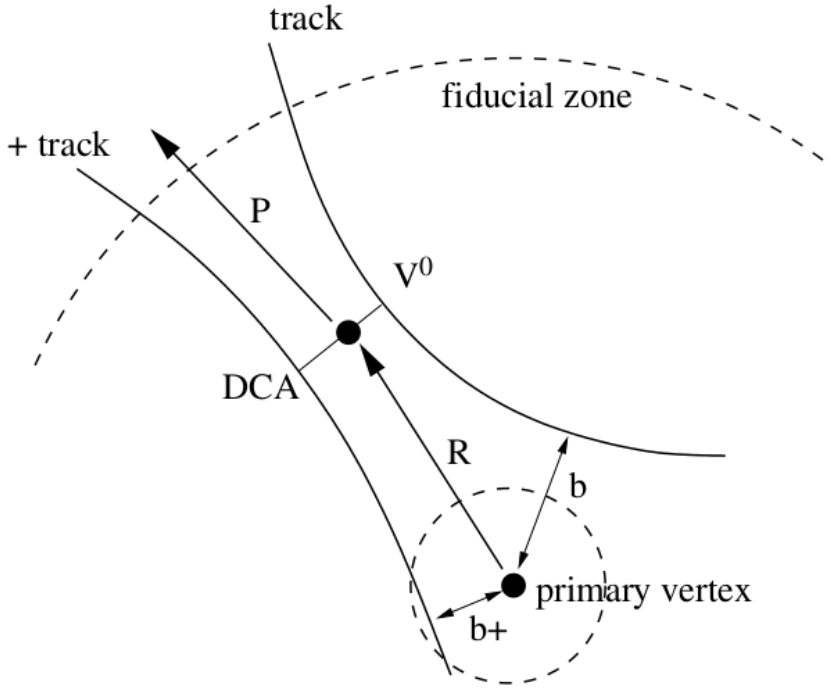

FIGURE 4.4: Visualization of the secondary vertex reconstruction.

Track & V^o cuts	**Meson Analysis p-Pb**
V^o-finder	On-the-Fly
minimum track $p_T$cut	$p_T track > 0.05$ GeV/c
findable clusters	$\frac{N_{\text{cluster TPC}}}{N_{\text{findable clusters}}} > 60\%$
Cut on conversion radius R_{conv}	5 cm $< R_{\text{conv}} <$180 cm
Cut on Z_{conv}	$\lvert Z_{\text{conv}} \rvert$ $<$ 240 cm.
Line cut for η_{cut} = 0.9	$R_{\text{conv}} > \lvert Z_{\text{conv}} \rvert \times ZR_{\text{Slope}} - Z_0$; Z_0 = 7 cm tan $(2 \times \arctan(\exp(-\eta_{\text{cut}})))$

TABLE 4.2: Standard cuts for the track and V^o selection for the p-Pb analysis.

mismatch between the actual detector and the MontCarlo simulations. The reason why the On-the-Fly V^o -finder is chosen as the standard method is the better conversion point resolution. To get the aimed track quality several requirements are made for the secondary tracks after the selection of the V^o candidates. They have to fulfill the TPC refit condition and to have a minimum track p_T of 50 MeV/c.The tracks should have more than 60% of all TPC clusters which would be theoretically possible, taking into account their point of origin and their inclination.

Moreover, there is a cut on the photon pseudorapidity (η) is applied. The pseudorapidity η of the particle is defined as the angle between the beam axis and the orientation of the 3- momentum vector of a particle in ZR-plane alone. In an asymmetric collision system like p-Pb, the two teams do not have the same collision energy due to the 2 in 1 magnet design of the LHC. This cause a difference between the laboratory system and the center of mass system cms which is not the case in other collision systems. For the p-Pb collisions at 8.16TeV the laboratory reference system is shifted by $\Delta y = 0.465$ units in rapidity relative to the cms in the direction of the photon beam.
The rapidity ranges used for this analysis are $-0.8 < y_{meson,lab} < 0.8$ and $-0.335 < y_{cms} < 1.265$ whereas the ranges for pseudorapidity $-0.9 < \eta_{\gamma,lab} < 0.9$. Additionally, the cut on the photon pseudorapidity (η) and the meson rapidity cut need to be modified in p-Pb collision system to make the asymmetric cuts possible in the laboratory system. For the pseudorapidity cut, the starting point of the trajectory is not taken into account which allows some photon candidates to pass it. Therefore, an additional condition has to be satisfied for the V^o candidates:

$$R_{\text{conv}} < |Z_{\text{conv}}| \times \tan(2.arctan(\exp(-\eta_{cut}))) - z_0, \tag{4.2}$$

where Z_0 = 7 cm, $\eta_{cut} = 0.9$ and the secondary vertices coordinates are determined independently from the primary vertex position with respect to the nominal center of the detector (X,Y,Z) = (0,0,0). To reconstruct secondary tracks with enough findable TPC clusters, secondary vertices with $R_{\text{conv}} > 180$ cm and $Z_{\text{conv}} > 240$ cm are rejected. Moreover, to reduce the Dalitz decays contamination all $V0$ candidates with $R_{\text{conv}} < 5$ cm are rejected. Since Dalitz decays are: $\pi^0 \rightarrow \gamma^*\gamma \rightarrow e^+e^-$ the e^+e^- pair produced from a virtual photon might be misidentified as a secondary e^+e^- pair. The contamination from Dalitz decay is negligible for conversion radii larger than 5 cm.
The reconstructed conversion points satisfy the selection criteria indicated in figure 4.5 as a spatial distribution in the x-y and the ZR- plane.

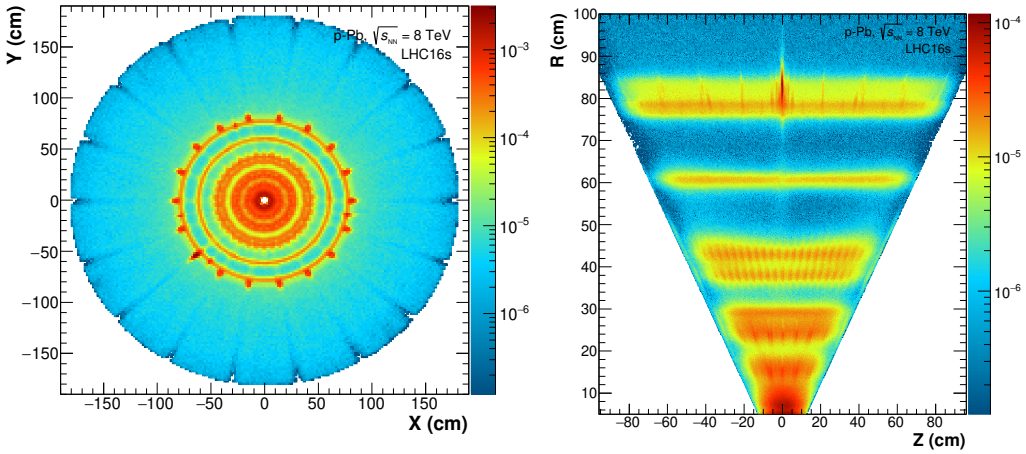

FIGURE 4.5: The reconstructed conversion points that passed the track and V^o selection criteria n the x-y plane (left) and ZR-plane (right).

4.2.2 Electron identification cuts

Not all the tracks that fulfill the track and V^o selection are electrons produced from photon conversions, they could also possibly be other particles decay products such as pions. All the applied electron identification and pion rejection cuts to the secondary tracks to select converted photons from V^o candidates. The different techniques used by the ALICE to identify electrons are:

- dE/dx in the ITS
- dE/dx in the TPC
- time-of-flight measurement with the TOF
- TR or dE/dx measurement in the TRD
- energy deposit in the calorimeters

For this analysis, the most important measurement is the dE/dx in the TPC. As the fraction of the secondary tracks in the other detectors is significantly lower and shows a significant loss in efficiency due to the very limited statistics. The cuts for electron identification used in this analysis are shown in table 4.3 the

PID cuts	Meson Analysis pPb
$n\sigma_e$ TPC dE/dx	$-3 < n\sigma_e < 5$
$n\sigma_\pi$ TPC dE/dx	0.4 GeV/c $< p <$ 100.0 GeV/c: $n\sigma_\pi > 0$

TABLE 4.3: Standard electron identification cuts for the p-Pb analysis.

cuts are applied in the same order and showing which part of the distribution left.

The main cut for electron identification is made around the electron energy loss dE/dx hypothesis in the TPC in terms of the standard deviations $n\sigma_{e,TPC}$. The cut is applied to be very tight to reduce contamination on electrons form Pions inside the remaining area. The p-Pb standard cut is to reject everything that does not lie within $-3n\sigma_{e^-,TPC}$ and $+5n\sigma_{e,TPC}$ around the electron line. A further pion rejection is performed by applying a cut around the pion hypothesis in terms of $(n\sigma_{\pi^0})$. This cut differs from the standard cut as it can be varied independently for low or high momentum tracks. This cut is applied over a momentum range 0.4 GeV/c $< p_{\mathrm{T}} <$ 100 GeV/c to reject everything below the pion line for the tracks.

In figure 4.6 the plot to the left shows electrons before all electron identification (PID) are applied whereas the plot to the right shows them after the cuts are applied and photon PID cuts can be seen. The corresponding Monte Carlo productions for the analyzed distribution by EPOS and DPMJET are shown in figure 4.6. There is a residual fraction of pions, protons, and kaons still visible after the cuts. This fraction will be accounted for in the systematic uncertainties.

4.2.3 Photon selection

After the track selection and electron identification cuts are applied, mainly electrons from the V^0 were selected and the selected photon sample reaches a purity of about 80%. Furthermore, improvement can be achieved by restricting the photon mass and the opening angle between the reconstructed photon

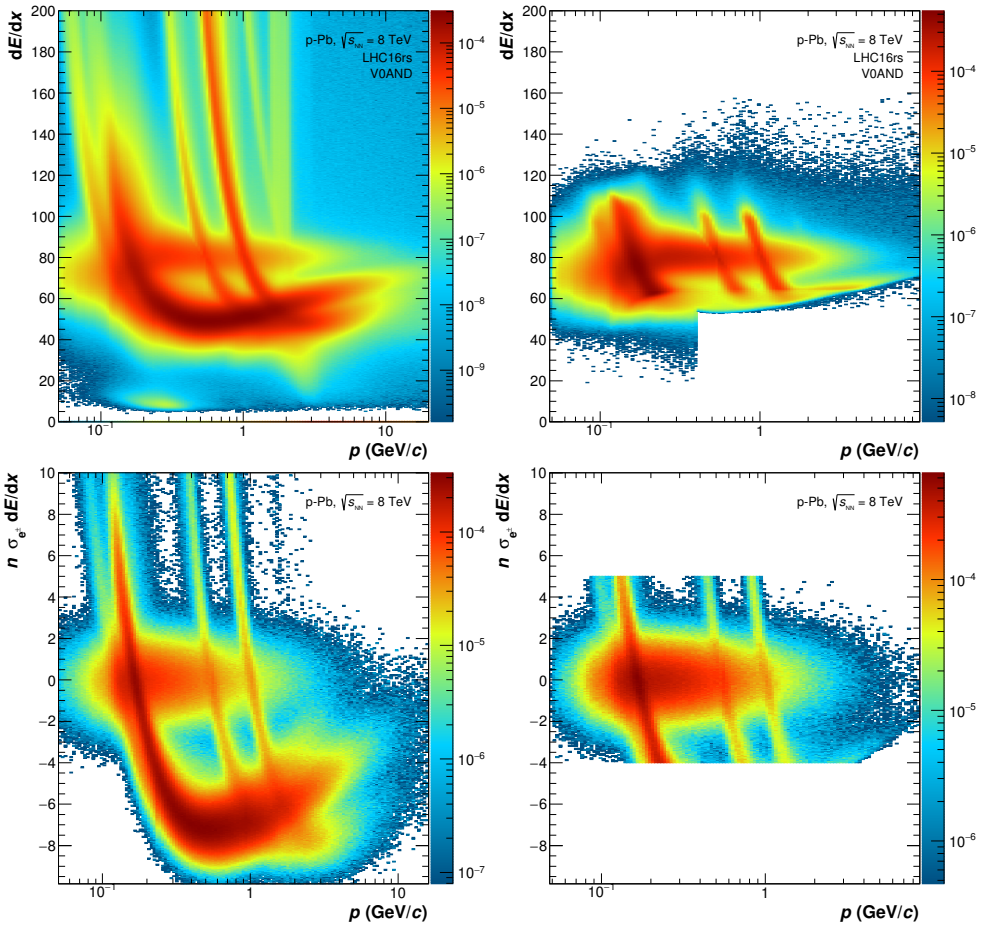

FIGURE 4.6: $n\sigma_{e^+,\mathrm{TPC}}\mathrm{d}E/\mathrm{d}x$ versus momentum for all positron candidates in data (left) and MC (right) after all track selection and electron identification cuts.

momentum vector and the vector between collision vertex and conversion point. This can be done indirectly via the AliROOT KF particle package [59] [60] which used for the photon reconstruction .
Additionally, a cut on the photon sample is used. This cut is χ^2/ndf and it is applied on a fit of a generic particle decay model based on the kalman filter method to a reconstructed V^o. Another cut applied on the photon sample is the ψ_{pair} cut. It is based on the opening angle of the photon-positron pair plane. This plane is perpendicular to the magnetic field and it is determined by the small opening angle of the tracks bended by the magnetic field. ψ_{pair} angle is illustrated in figure 4.7 and the formula used for the ψ_{pair} cut is given by

$$\psi_{(pair)} = \arcsin\left(\frac{\Delta\theta}{\xi_{pair}}\right) \tag{4.3}$$

where $\Delta\theta = \theta_{e^-} - \theta_{e^+}$ angle is in the polar direction. $\psi pair$ is the arcsine of the ratio between the difference of the angles of the two daughter tracks with the z-axis and the angle between the propagated to a radius. All the tracks are propagated to a radius of 50 cm from the conversion point and

$$\xi_{(pair)} = arcos\left(\frac{\overrightarrow{p_{e^-}}.\overrightarrow{p_{e^+}}}{|\overrightarrow{p_{e^-}}|.|\overrightarrow{p_{e^+}}|}\right) \tag{4.4}$$

A two dimensional cut combined from χ^2/ndf and ψ_{pair} is applied for this standard analysis. The V^o candidates with a given $\chi^2_{\gamma,max}$ and $\psi_{pair,max}$ from table 4.4 need to satisfy $|\psi_{pair}| < \frac{-\psi_{pair,max}}{\chi^2_{\gamma,max}}.\chi^2_\gamma + \psi_{pair,max}$ otherwise they are rejected.

Photon selection cuts	**Meson Analysis p-Pb**
$\chi^2_{\gamma,max}$ /ndf	$= 30$
$\psi_{pair,max}$	$= 0.05$
$(\frac{\alpha}{0.95GeV/c})^2 + (\frac{q_T}{q_{T,max}})^2$	< 1

TABLE 4.4: Standard photon selection cuts for the p-Pb analysis.

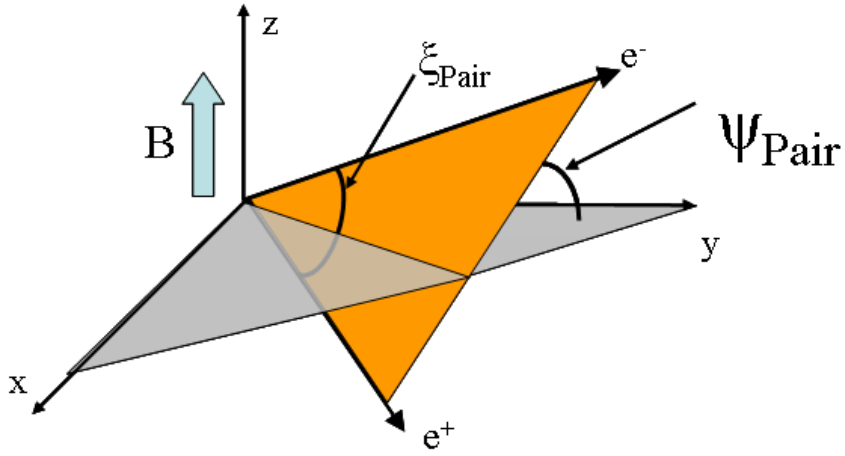

FIGURE 4.7: Visualization of the ψ_{pair} angle.

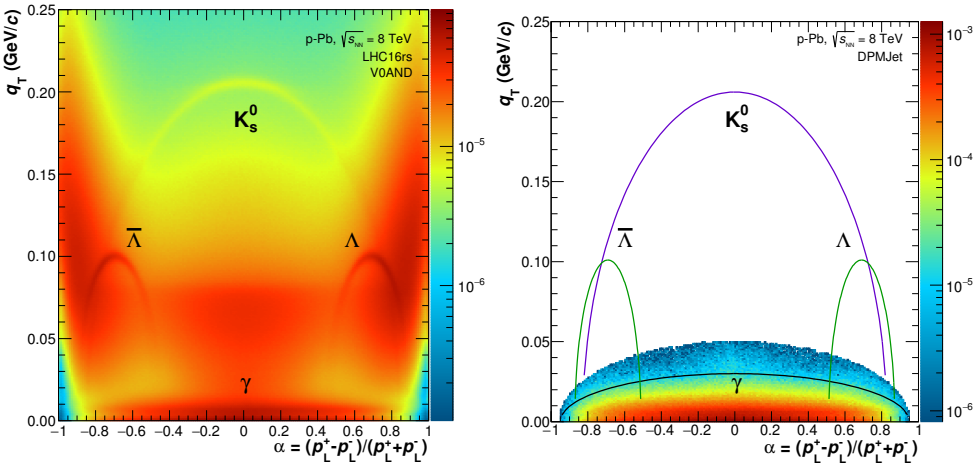

FIGURE 4.8: Armenteros-Podolanski plot for all *Vo* candidates after the track selection (left) and after all electron identification and photon selection cuts (right).

Another cut is added to χ^2/ndf and ψ_{pair} which is the elliptical cut in $q_t = p \times \sin\theta_{mother-daughter}$ and the α of the Armenteros-Podolanski plot [61]. q_t is used to exclude the remaining k^0_s, Λ, and π. It is defined as the projection of the momentum of the daughter particle with respect to the mother particle i.e. the transverse direction.

The Armenteros-Podolanski plot 4.8 is showing q_t versus the longitudinal momentum asymmetry $(\alpha = (P^+_L - P^-_L)/(P^+_L - +P^-_L))$. The q_t of the converted photons is close to zero as the daughter particles of the photon have a very small opening angle and this is the fly in the same direction as the mother particles.

Therefore, using the q_t cut allows having a clean photon sample

by easily distinguishing heavier particles which show larger q_t while particles with the same mass i.e. photons show symmetry of the distribution in the Armenteros-Podolanski plot in figure 4.8. Unlike distributions for Λ and $\bar{\Lambda}$ are shifted to positive and negative α, respectively. The Armenteros-Podolanski plot in figure 4.8 shows all the V^o candidates after applying the track selection (left) and the electron selection (right). Only real photons remained after all other V^o candidates are excluded. The created photon sample is very clean.

4.3 Neutral Meson Reconstruction

The neutral mesons are reconstructed by combining photons candidates from the selected V0 sample with the criteria discussed in 4.2. Photon pairs have invariant mass calculated using the equation:

$$M_{\gamma\gamma} = \sqrt{2E_{\gamma_1}E_{\gamma_2}(1-\cos\theta_{12})}, \tag{4.5}$$

where $E_{\gamma_{1,2}}$ represent the energies of the two photons and θ_{12} is the opening angle between them in the laboratory frame. The way neutral mesons are determined is that they show excess in the invariant mass plot at their respective mass, 0.135 GeV/c^2 for the π^0 meson and 0.548 GeV/c^2 for the η meson. The invariant mass plots show the distribution of the photon pairs about the rest mass of the π^0 and η meson. The π^0 meson can be extracted in high and low p_{T} as it is very distinguishable from the background while extracting η meson is limited by the background at low p_{T} due to low statistics. All photons of one event are paired and assembled to create this pure combinatorial background using the following special techniques.

4.3.1 Event Mixing method

The event mixing technique aims to remove all the correlations between photons to create a pure combinatorial background by mixing photon pairs from different events. The shape of the

background depends on the multiplicity in the event, the primary vertex position in Z and the transverse momentum. Therefore, the photons candidates are binned in different multiplicity bins.

4.3.2 Signal Extraction

The extraction of the meson signal requires that the invariant mass of the photon pairs to be calculated in different p_{T} bins. For the π^0 analysis the transverse momentum ranges from 0.3 GeV/c up to 12 GeV/c. While η analysis covers p_{T} range of 0.7 GeV/c to 4 GeV/c the plots for all the p_{T} bins can be seen in the appendix A.1. At first, the calculation is done for photons from the same event. Afterwards, it is done for photons from mixed events for background subtraction. The mixed event background distribution should be subtracted. It can be subtracted to the left or to the right side of the peak, as close as possible without going into it. The invariant mass signal is extracted after normalizing the background distribution to the invariant mass distribution then, subtracting the background. However, the invariant mass distribution will still have some residual background as can be seen in figure 4.9 left and right. Then, fitting the subtracted signal with Gaussian function combined with an exponential low-energy tail on the let side which accounts for electron Bremsstrahlung. Further, the remaining background is described by a linear part if the combinatorial background does not describe the background under the peak. The fit function is represented by:

$$y = A \cdot \left(G(M_{\gamma\gamma}) + \exp\left(\frac{M_{\gamma\gamma} - M_{\pi^0(\eta)}}{\lambda} \right) (1 - G(M_{\gamma\gamma}))\theta(M_{\gamma\gamma} - M_{\pi^0(\eta)}) \right) + B + C \cdot M_{\gamma\gamma} \quad (4.6)$$

with,

$$G = \exp\left(-0.5 \left(\frac{M_{\gamma\gamma} - M_{\pi^0(\eta)}}{\sigma_{M_{\gamma\gamma}}} \right)^2 \right) \quad (4.7)$$

Here, G is a Gaussian function with the width σ, the amplitude A and the mean position $M_{\pi^0(\eta)}$, which is determined by reconstructing the mass position of the π^0 or η meson. λ is

a parameter that represents the inverse slope of the exponential function which is set to be zero by the heavy side function $\theta(M_{\gamma\gamma} - M_{\pi^0(\eta)})$. B and C are the parameters of the linear function. Figure 4.9 shows the mixed event combinatorial background on the left side with the blue line and the peak fit on the right side with the cyan line.

The invariant mass obtained as well as the full width half maxi-

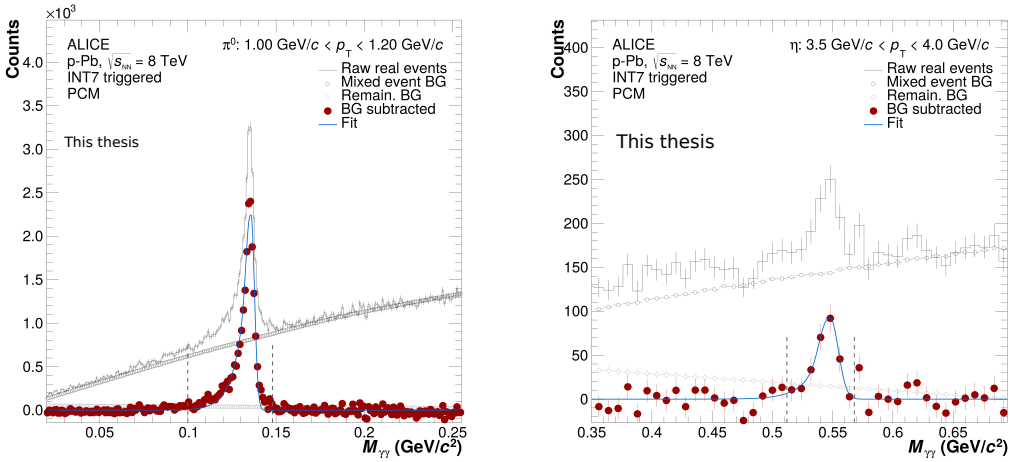

FIGURE 4.9: Invariant mass distribution for an example bin with the p_T range of 1.2 GeVc to 1.4 GeVc for Pion. The data including background is plotted in black and with background subtracted in red. In the (left) plot, the combinatorial background for π^0 and to the (right) for η from the event mixing method is drawn in gray and the linear fit to the residual background is shown in pale gray. In both plots, the fit function mass peak is drawn in cyan.

mum (FWHM) of the fitted mass peak of the meson in respective p_T bin as shown in figure 4.10. The ratio of the mass positions between data and MC is studied to ensure they agree as shown in figure 4.10. Afterward, the invariant mass is integrated to extract the meson yield, the invariant mass is subtracted around the fitted meson mass $M_{\pi^0,\eta}$.

The integration range for the Pion is $(M_{\pi^0} - 0.035\,\mathrm{GeVc}^2, M_{\pi^0} + 0.012\,\mathrm{GeVc}^2)$ which coincides to $(-11\langle n\sigma_\pi\rangle, 4\langle n\sigma_\pi\rangle)$ around M_{π^0}. To encounter the bremsstrahlung tail on the left side of the distribution an asymmetric range is needed. The formula used for Pion raw yield is given by:

$$N_{raw}^{\pi^0} = \int_{M_{\pi^0}-0.035\mathrm{GeV/c^2}}^{M_{\pi^0}+0.012\mathrm{GeV/c^2}} (N^{\gamma\gamma} - N^{\mathrm{comb.BG}})\mathrm{d}M_{\gamma\gamma} - \int_{M_{\pi^0}-0.035\mathrm{GeV/c^2}}^{M_{\pi^0}+0.012\mathrm{GeV/c^2}} (B + C \cdot M_{\gamma\gamma})\mathrm{d}M_{\gamma\gamma} \tag{4.8}$$

While in case of eta, the integration range is is $(M_\eta - 0.036\,\mathrm{GeVc^2}, M_\eta + 0.018\,\mathrm{GeVc^2})$ which coincides to $(-6\langle n\sigma_\eta\rangle, 3\langle n\sigma_\eta\rangle)$ around M_η. The formula used for Pion raw yield is given by:

$$N_{raw}^{\eta} = \int_{M_{\eta}-0.036\mathrm{GeV/c^2}}^{M_{\eta}+0.018\mathrm{GeV/c^2}} (N^{\gamma\gamma} - N^{\mathrm{comb.BG}})\mathrm{d}M_{\gamma\gamma} - \int_{M_{\eta}-0.036\mathrm{GeV/c^2}}^{M_{\eta}+0.018\mathrm{GeV/c^2}} (B + C \cdot M_{\gamma\gamma})\mathrm{d}M_{\gamma\gamma} \tag{4.9}$$

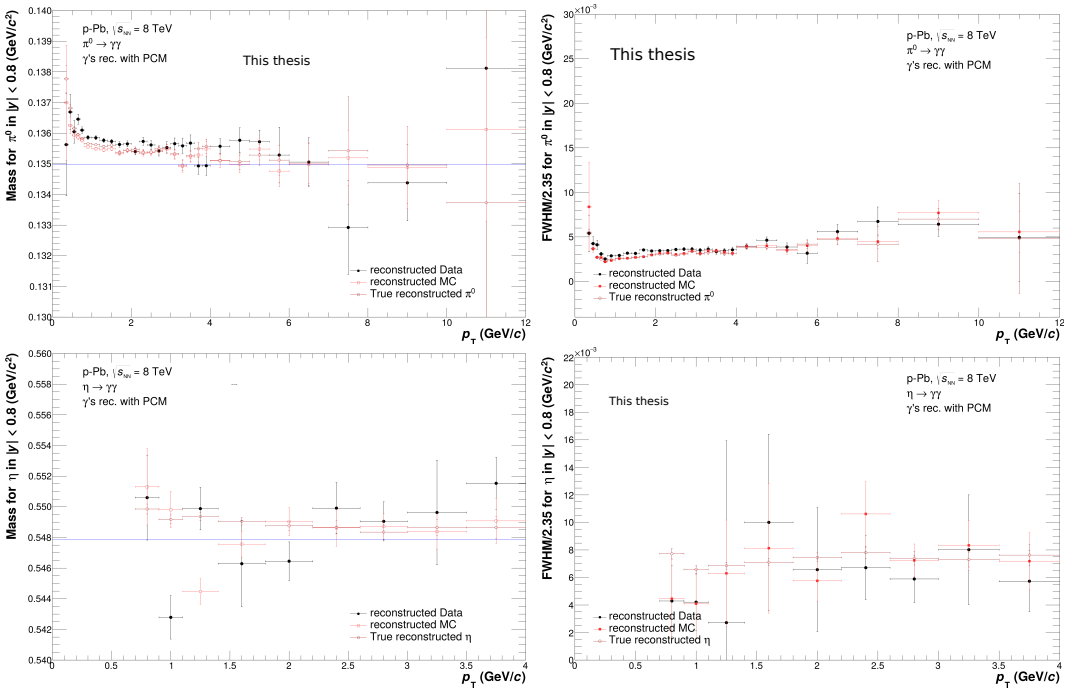

FIGURE 4.10: Mass and FWHM of the neutral pion (**left**) and the eta meson (**right**) of the respective mass peaks depending on the p_T bin. Points from data are shown in black while acMC points are shown in red. The gray line indicates the nominal meson mass.

The raw yield for π^0 and η are shown in figure 4.11 normalized by the number of events N_{ev} presented in table 4.1 and by the bin width in p_T for minimum bias and different multiplicity bins. The statistics and background limit the transverse momentum in high p_T and low p_T respectively.

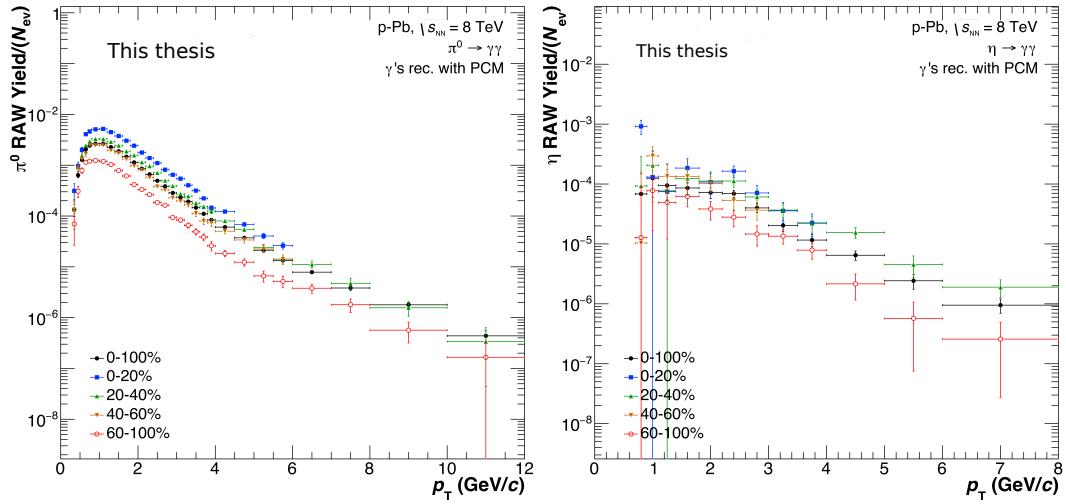

FIGURE 4.11: Raw yield of the π^0 (left) and Eta meson (right) for minimum bias and different multiple bins. The yield is normalized to the number of events N_{evt} and the spectra are divided by the bin width in p_{T} .

4.4 Meson Spectra Corrections

There are some corrections that need to be applied to the raw yield of the mesons to get the real yield of π^0 and η. At first, all the secondary π^0 mesons produced from weak decays or hadronic interactions in the detector material should be subtracted from the reconstructed raw neutral pion yield. Then, an efficiency and a geometrical acceptance corrections are calculated from MC and removed. Another, important factor to be corrected is the contribution from the out of bunch pile up π^0 and η reconstructed in the TPC. Finally, the spectra will be corrected for the finite bin width in transverse momentum.

4.4.1 Correction for Secondary Neutral Pions

The π^0 originating from the decay $k_s^o \rightarrow \pi^0\pi^0$ represents the largest contribution of secondary π^0 with branching ratio of BR $= 30.7\%$. Nevertheless, the secondary fraction at low p_{T} about 6% while at high p_{T} lies below 1%.
The way the fraction of secondary neutral pions from all sources

are evaluated is by using the same MC production as for the efficiencies and acceptance correction. In order to obtain the secondary yield, the fractions of all secondary sources are multiplied with the raw neutral pion yield. Then, the resulting estimated secondary raw yield is subtracted from the raw yield. The function of secondary pions coming from several sources are shown in figure 4.12 where all secondary interactions and material interactions producing neutral pions are indicated by "Rest". The material interactions are the dominant component with more than 99%.

Further, particles secondary contributions from Λ, $\Lambda \rightarrow n\pi^0$ and $k_L^0 \rightarrow \pi_L^0,^+ \pi^0,^- \pi^0$ are seen in the figure in orange and Cyan receptively.
Then, the final reconstructed yield according to this method is subtracted from the raw yield is illustrated in figure 4.12.

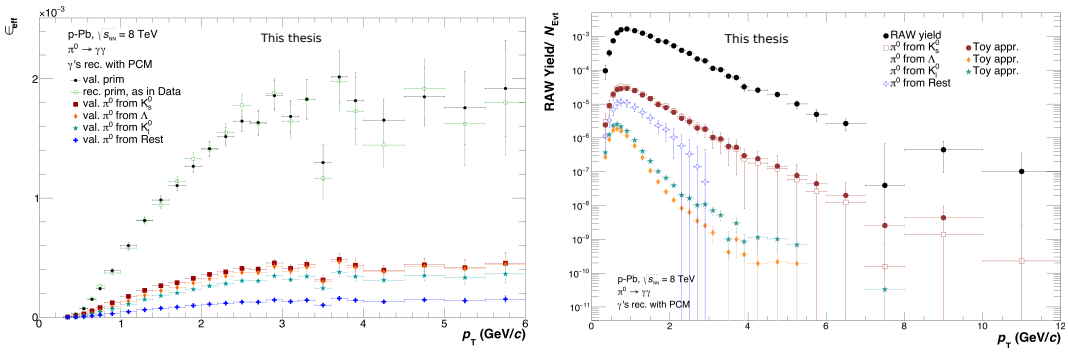

FIGURE 4.12: The efficiency of the reconstructed secondary Pion mesons from different sources to reconstructed neutral pions (left) and the secondary raw yield (right).

4.4.2 Acceptance and Efficiency Correction

The second correction to be applied to the raw yield after the correction for secondaries is to correct for the detector acceptance and efficiency. The way to do this is by using the Monte Carlo simulations, which supply more information about particles in the collision.

The geometrical acceptance $A_{\pi^0(\eta)}$ is defined as the ratio between the $\pi^0(\eta)$ mesons within rapidity range $|y| < 0.8$ $(N_{\pi^0(\eta),|y|<0.8})$

whose daughter particles are within an acceptance of $|\eta| < 0.9$ as a safety margin to avoid edge effects and the total number of $\pi^0(\eta)$ mesons in the same rapidity range. The geometrical acceptance is a property of the detector depending on the transverse momentum.

$$A_{\pi^0(\eta)} = \frac{N_{\pi^0(\eta),|y|<0.8} \text{ with daughter particles within } |\eta_\gamma| < 0.9}{N_{\pi^0(\eta),|y|<0.8}} \tag{4.10}$$

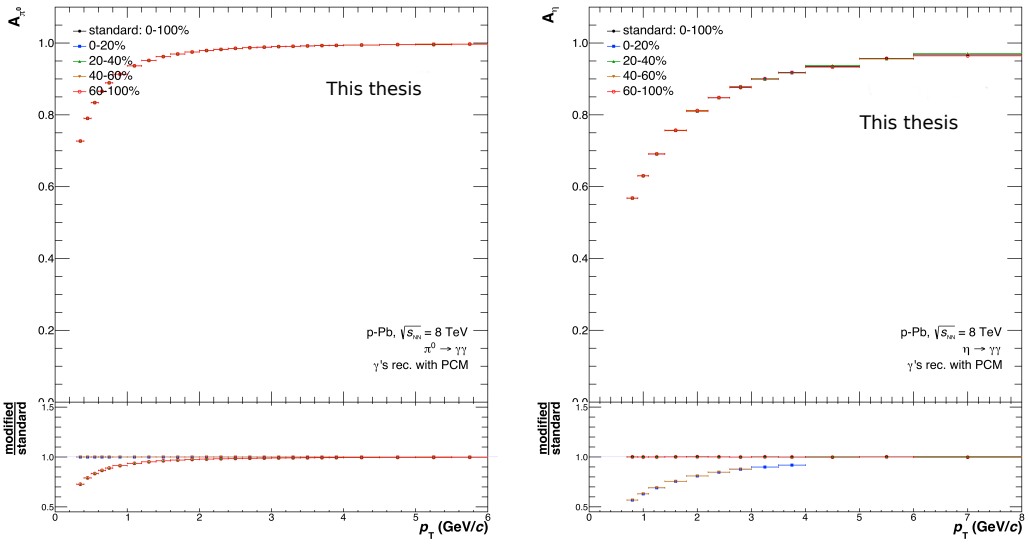

FIGURE 4.13: Geometrical acceptance for minimum bias and different multiplicity bins for π^0 (left) for η (right).The term standard refers to minimum bias and the term modified refers to different multiplicity bins

Figure 4.13 shows the geometrical acceptance for π^0 mesons (left) and η meson (right). The neutral pion and eta mesons have different opening angle distributions which cause a difference for both mesons depending on p_{T} .
The reconstruction efficiency is determined by finding the ratio of the photon pair that with Monte Carlo information to the selected $\pi^0(\eta)$ meson within $|y| < 0.8$ whose daughter particles

are within the acceptance of $|\eta| < 0.9$. Therefore, the combinatorial background is suppressed. The reconstruction efficiency is defined by:

$$\epsilon_{\text{reco, }\pi^0(\eta)} = \frac{\text{MC reconstructed } N_{\pi^0(\eta),\text{primary sec}}}{N_{\pi^0(\eta),|y|<y_{\max}}, \text{ daughter particles within } |\eta_\gamma| < 0.9_{(\text{pt,MC})}} \quad (4.11)$$

Figure 4.14 shows the reconstruction efficiency for both π^0 and η.
There are two factors to determine the reconstruction efficiency, the first one is the conversion probability of photons depending on the transverse momentum p_{T} and the interaction with the detector material. The second factor is the efficiency of reconstructing photons as all photons and their conversion products have to be in the acceptance of the detector in order to be reconstructed at the TPC. Therefore, the efficiency rises slowly until it levels out at 2 GeV/c transverse momentum. A conversion probability of $\approx$ 8.6% combined with reconstruction efficiency of $\approx$ 68% limits the reconstruction efficiency for mesons to the maximum of 0.34%, this value can not reach by simulation due to light photons cuts for this analysis as seen in figure 4.14.

4.4.3 Correction for Neutral Mesons from Out-of-Bunch Pileup

The TPC has a drift velocity of charges about 20.7cm/μs with a corresponding readout time of about 92μs. The long readout leads to the large integration time of the TPC combined with the LHC filling scheme which causes overlapping of events in the TPC. Therefore, an out of bunch pileup rejection is required.
To subtract this pileup the distance of closest approach is used. The distance in the beam direction(z) called DCA_z and identified by it's Gaussian shape. The dca_z distribution for an example p_{T} bin can be seen in figure 4.15.
The conversion method is able to reconstruct three different types of photons coming in three different categories:

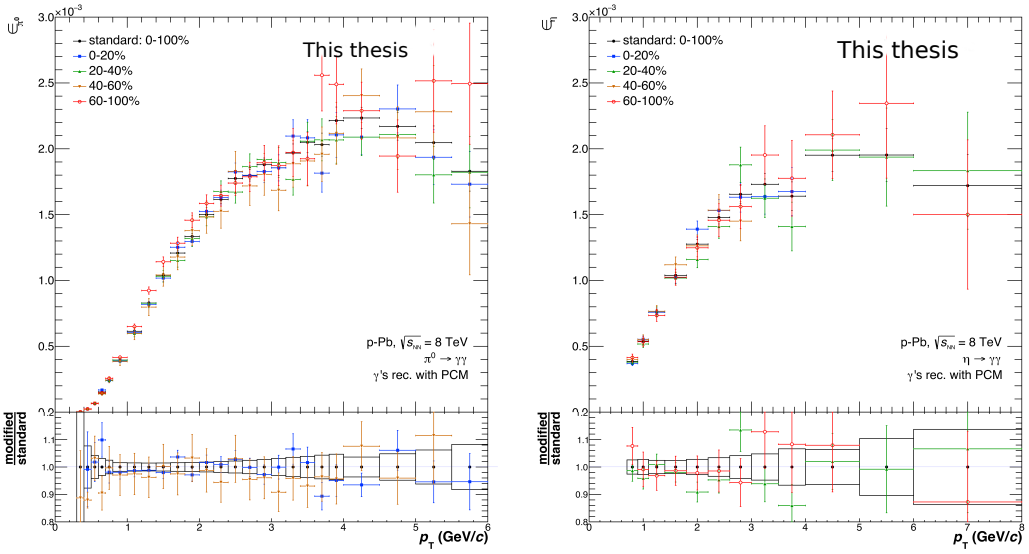

FIGURE 4.14: The reconstruction efficiency of π^0 (right) and for η (left). The term standard refers to minimum bias and the term modified refers to different multiplicity bins .

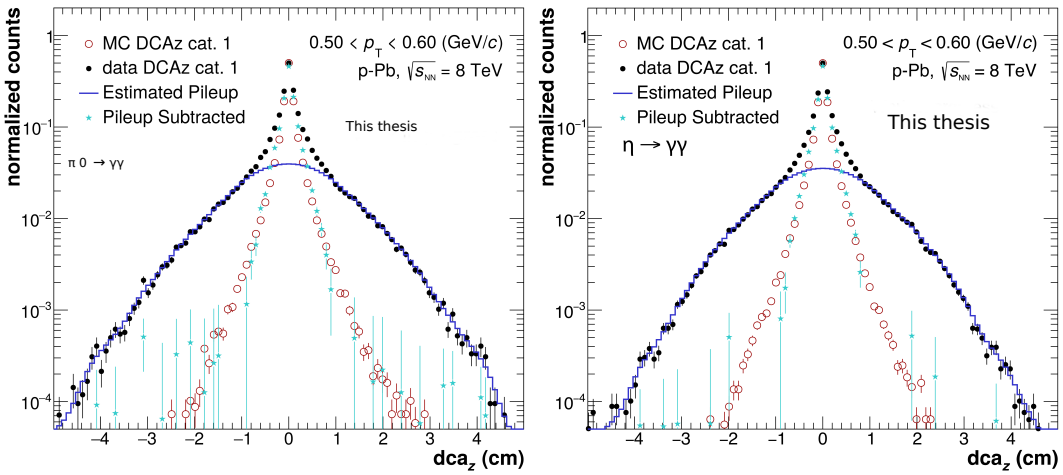

FIGURE 4.15: Example DCA_z distribution for 0.5 < p_T< 0.6 GeV/c. the data is shown in black, the ShowBackground based background description in blue, the background subtracted data in cyan and Monte Carlo in red. The Pileup contribution determined by fitting the DCA_z distribution under the peak.

1. both legs are TPC only tracks (case for all photons with $RConv \geq 50$ cm)
2. one of the electrons has at least 2 ITS hits

3. both legs have at least 2 ITS hits

The contribution of each category varies from one to another depending on momentum. The resulting correction factor for the minimum bias analysis shown in figure 4.16 and the one for different multiplicity bins is shown in the appendix B.1.

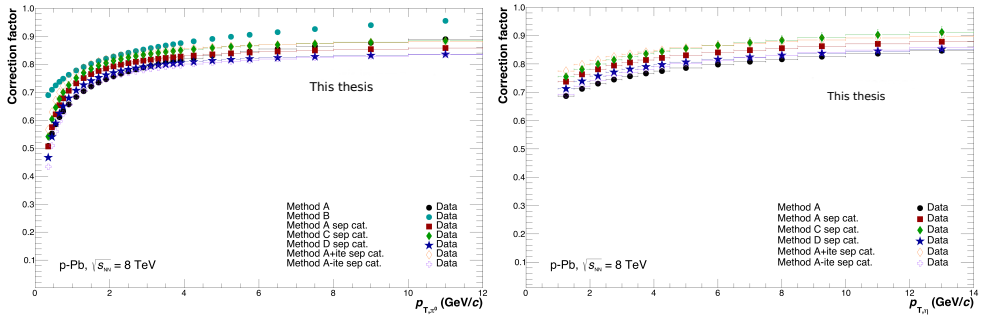

FIGURE 4.16: The resulting correction factor for the minimum bias for π^0 (left) and for η (right).

4.4.4 Correction for Finite Bin Width

The transverse momentum binning of the π^0 and η meson spectra has different width which increases for higher p_{T}. Therefore, the raw yield should be corrected for the true bin value. The spectrum is steeply falling due the fact that the yield in one of those bins is not at the bin center. But, the data points are shifted horizontally to represent the real transverse momentum at the bin center while shifting the yield vertically is usually used for ratios like R_{pA} or η/π^0.
For both cases, the yields are shifted by assuming a Tsallis function to estimate the underlying spectrum.

$$E\frac{d^3N}{dp^3} = \frac{1}{2\pi p_{\mathrm{T}}}\frac{d^3N}{dy dp_{\mathrm{T}}} = \frac{1}{2\pi}\frac{dN}{dy}\frac{(n-1)(n-2)}{nT^{\mathrm{eff}}(nT^{\mathrm{eff}}+m(n-2))}\left(1+\frac{\sqrt{p_T^2+m^2}-m}{nT^{\mathrm{eff}}}\right)^{-n} \quad (4.12)$$

The parameter m is the measured meson mass and $\sqrt{m^2+p_T^2} = m_T$ is the transverse mass. The parameters dN/dy, T^{eff} and n are determined using the fit. This correction depends on the bin width and steepness of the underlying spectrum.

4.5 Systematic uncertainty Evaluation

This section will present the different sources causing systematic uncertainties when the meson yield is evaluated.
The systematic uncertainty is an important part of the analysis estimated by varying the cuts performed to select the tracks, electrons, photons, clusters, and mesons. This variation is sampling the underlying Gaussian distribution (i.e. variation of the pion rejection cut) or make access to the maximum deviation (i.e. the variation of the single track momentum cut). Each cut is varied once a time to evaluate its contribution, then calculate the difference for the fully corrected spectra in all p_{T} bins.

$$\Delta(p_{\mathrm{T}}) = \left(\frac{\mathrm{d}^2N}{\mathrm{d}y\mathrm{d}p_{\mathrm{T}}}\right)_{\text{modified}}(p_{\mathrm{T}}) - \left(\frac{\mathrm{d}^2N}{\mathrm{d}y\mathrm{d}p_{\mathrm{T}}}\right)_{\text{standard}}(p_{\mathrm{T}}) \quad (4.13)$$

$$\sigma_{\Delta}(p_{\mathrm{T}}) = \sqrt{\left|\sigma^2\left(\frac{\mathrm{d}^2N}{\mathrm{d}y\mathrm{d}p_{\mathrm{T}}}\right)_{\text{modified}}(p_{\mathrm{T}}) - \sigma^2\left(\frac{\mathrm{d}^2N}{\mathrm{d}y\mathrm{d}p_{\mathrm{T}}}\right)_{\text{standard}}(p_{\mathrm{T}})\right|}, \quad (4.14)$$

where $\sigma_{\Delta}(p_T)$ is the statistical uncertainty for fully corrected spectrum and has been calculated using equation 4.13 and checked afterwards whether the uncertainty is significant due to statistical fluctuations. The uncertainty calculated bin by bin by varying the cuts from the standard cut and then take the average of the maximum deviation as the systematic uncertainty. The cut variations preformed to determine the systematic uncertainty for p-Pb at $\sqrt{s} = 8$TeV is listed in detail in table 4.5 below. Figure 4.17 and figure 4.18 show the systematic uncertainty for π^0 and η analysis. Quadratic sum is the total systematic uncertainty of all sources plotted in black.

The sources of systematic uncertainty will be discussed below:

Material Budget

The Conversion probability of the reconstructed photons is

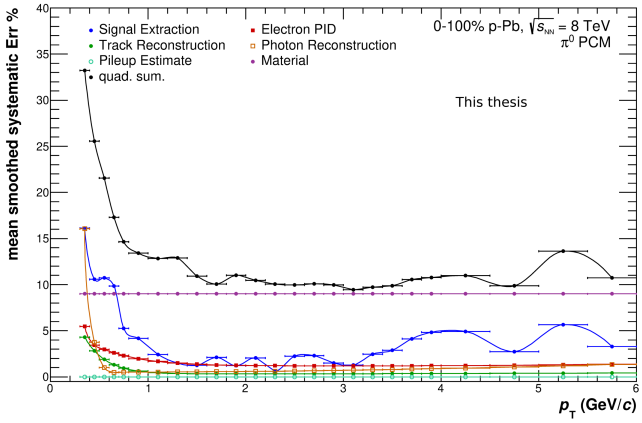

FIGURE 4.17: Systematic uncertainties of the π^0 shown in colored points each uncertainty source individually. All uncertainties has been smoothed using a polynomial or exponential function smooth statistical fluctuations. The final systematic uncertainty is represented in black points.

mainly dependent on the material budget of the ALICE detector. Therefore, the material budget has been studied in detail with the PCM method [28]. The material budget represents the largest source of systematic uncertainty with 9% for both photons. The systematic uncertainty of the material budget is based on the R distribution of the photon candidates, therefore, no variations are applied to the R cut to avoid double counting in systematic uncertainty.

Signal extraction The variation in the energy symmetry α cut of the two photons combined with the signal extraction error contribute to this source of uncertainty. The signal extraction uncertainty evaluated by varying the integration window for the signal extraction and the range for the normalization of the background. The variations of the integration window for both mesons are shown in table 4.5. The contribution of the yield extraction to the total systematic uncertainty is between 2-16%.

Track reconstruction This category combines the systematic uncertainties coming from the variations of the TPC cluster over findable cluster cut together with the minimum transverse momentum cut contribute to this source of systematic uncertainty. The strong contribution from this source to the

systematic uncertainty comes at low p_{T} whereas, at high p_{T} it contributes with only $1-4\%$.

Electron PID

The cuts considered in this category are the electron identification or pion rejection in addition all σ cuts on the TPC dE/dx. This category contributes with $2-5\%$ of π^0 systematic uncertainty and $\eta's$ dependently on p_{T}.

Photon Reconstruction

This category involves the following: cuts on q_T, and the two dimensional cut on χ^2 and ψ_{pair}. This category is strongly dependent on p_{T} contributing with $2-6\%$ to the total π^0 systematic uncertainty. While the contribution for the η systematic uncertainty is strongly dependent on p_{T} in the range 2 to 12%.

Pileup Estimate

Two types of pileup contribute to this category, the SPD in-bunch pileup correction, and the out-of-bunch pileup correction. The uncertainty is estimated by applying several variations to the DCA_z. The uncertainty from this source is approximately 1%

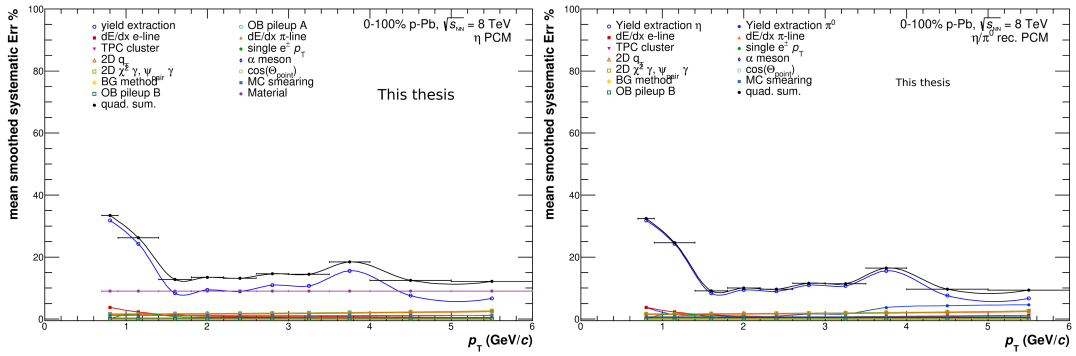

FIGURE 4.18: Systematic uncertainties of the η (left) and η/π^0 (right) shown in colored points each uncertainty source individually. All uncertainties has been smoothed using a polynomial or exponential function smooth statistical fluctuations. The final systematic uncertainty is represented in black points.

Quantity	Standard	Cut Variation1	Cut Variation2	Cut Variation3
single p_{T} $e^{\pm}$	> 0.05 GeV/c	> 0.075 GeV/c	> 0.1 GeV/c	
min TPC clust./ find. TPC clust.	$> 60\%$	$> 35\%$	$> 70\%$	
dE/dx e-line				
$\sigma_{\mathrm{d}E/\mathrm{d}x,e}$	$-3 < n\sigma_e < 5$	$-4 < n\sigma_e < 5$	$-2.5 < n\sigma_e < 4$	
dE/dx π-line				
$p_{\mathrm{min},\pi\mathrm{rej.}}$	0.4 GeV/c	0.5 GeV/c		
$p_{\mathrm{max},\pi\mathrm{rej.}}$	3.5 GeV/c	5.0 GeV/c		
$n\sigma_{\mathrm{d}E/\mathrm{d}x,\pi}$ rej.	$n\sigma_\pi > 1$	$n\sigma_\pi > 2$	$n\sigma_\pi > 0$	
high p $\sigma_{\mathrm{d}E/\mathrm{d}x,\pi}$ rej.	$n\sigma_\pi > -10$			
$q_{\mathrm{T,max}}$	< 0.05 GeV/c (2D)	< 0.07 GeV/c (1D)	< 0.03 GeV/c (2D)	< 0.05 GeV/c (1D)
χ^2 γ	< 30	< 50	< 20	< 30
Ψ_{pair}	< 0.1 (2D)	< 0.2 (2D)	< 0.05 (2D)	< 0.1 (1D)
α **meson**	< 1	< 0.85		

TABLE 4.5: Variations for the systematic uncertainty evaluation in p-Pb collisions at $\sqrt{s_{NN}} = 8.16$TeV. The "Standard" column is for the standard cut and the "Cut variation" columns show the variations applied to the standard cut. To estimate the systematic uncertainty only one cut is changed at a time. While this is not the case for $\chi^2\gamma$ and ψ_{pair} cut as they are correlated).

Chapter 5

Results

This chapter will present the reconstructed and corrected meson yield. Further, the η/π^0 ratio and the nuclear modification factors will be presented for minimum bias events and different multiplicity classes.

5.1 Yields of neutral pions and eta mesons

The results of the PCM analysis for minimum bias events and different multiplicity classes are presented. The corrected yield for neutral pions and eta mesons are shown in figure 5.1 for minimum bias and different multiplicities in figure 5.2. All yields are not corrected for finite bin width i.e. all the values are the average values of the presented bin and not the value at the center of the bin. The vertical error bars are the statistical uncertainties, the horizontal error bars represent the width of the each bin and systematic uncertainties are shown as boxes. The yields are normalized to the number of accepted events.

5.1.1 η/π^0

The η/π^0 ratio for minimum bias is presented in figure 5.3 and figure 5.4 shows the ratio for different multiplicities. The ratio is calculated by reconstructing π^0 with the same binning as η. Therefore, common systematic uncertainties like the material budget will cancel out. The p_{T} range is limited by the available statistics. Systematic uncertainties are shown as boxes and statistical errors shown as error bars. No significant difference is observed between the minimum bias and the multiplicity dependent ratio. The importance of this ratio is to study the influence of the content of quarks on the fragmentation [62].

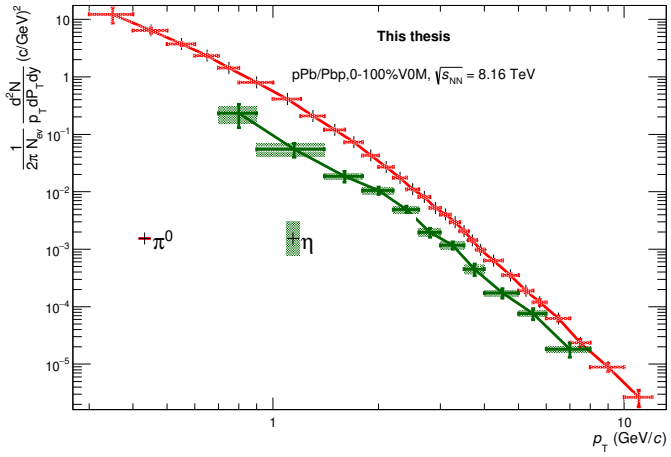

FIGURE 5.1: Corrected yield for both mesons π^0 (top) η (bottom) for minimum bias. Systematic uncertainties are shown as boxes and statistical uncertainties are drawn as vertical error bars.

5.1.2 Nuclear modification factor

The nuclear modification factor R_{pPb} is the ratio of the measured meson yield in p-Pb to the cross section of pp, scaled using the number of binary collisions N_{Coll}.

$$R_{pPb}(p_{\mathrm{T}}) = \frac{d^2N^{pPb}_{\pi^0,\eta}/dydp_{\mathrm{T}}}{\langle N_{coll}\rangle d^2N^{pp}_{\pi^0,\eta}/dydp_{\mathrm{T}}} \tag{5.1}$$

The ratio is expected to be consistent with unity at high p_{T}. However, it turned out to be inconsistent with unity for lower transverse momenta as the N_{coll} does not hold due to nuclear matter effects.

The R_{pPb} for both mesons is calculated by using the pp spectrum at $\sqrt{s_{NN}} = 8\,\mathrm{TeV}$ as a reference. The pp spectra compared to an interpolated spectrum shown in appendix D.1. No significant difference was observed between the two spectra, therefore, the difference in energies of the pp reference spectrum and p-Pb spectrum is therefore not significant. The number of binary collisions N_{coll} for p-Pb collisions at $\sqrt{s_{NN}} = 5.2\,\mathrm{TeV}$ is used as this number at $\sqrt{s_{NN}} = 8.16\mathrm{TeV}$ is not yet available. As the spectrum for p-Pb has different binning than the spectrum of pp, a Tsallis fit [63] of the pp spectrum has been used instead. The

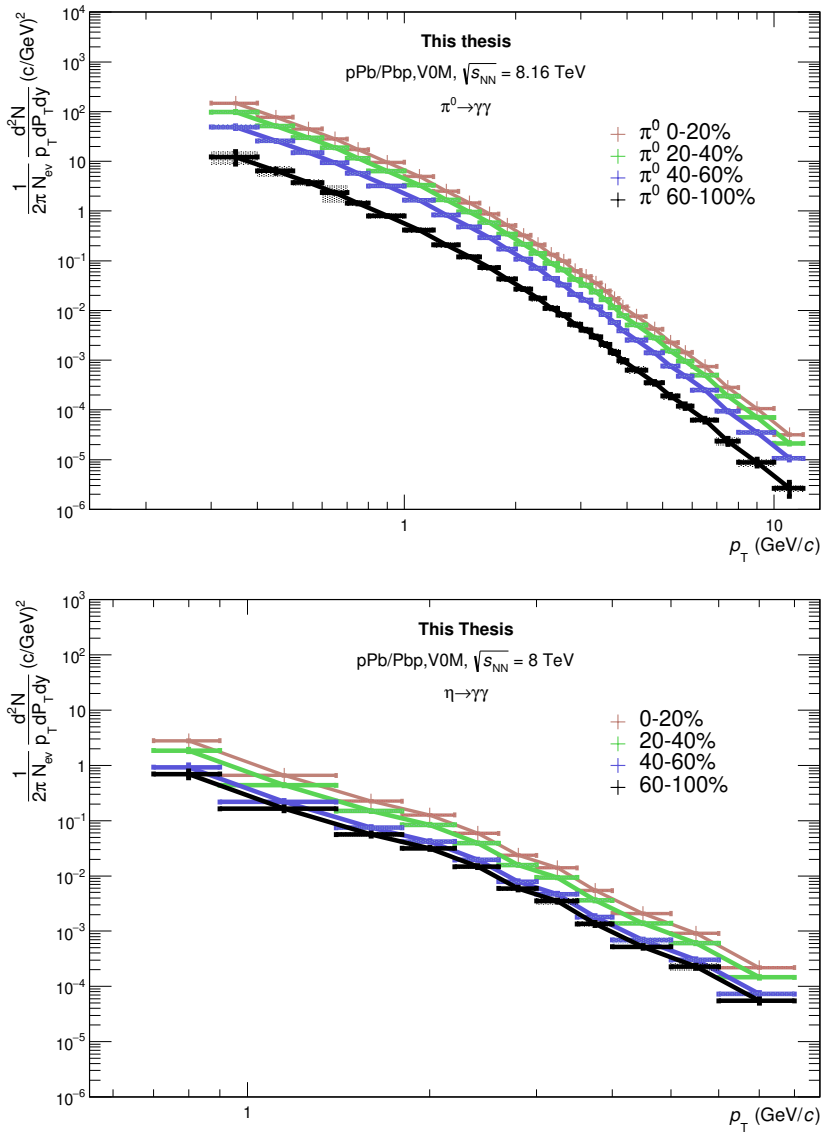

FIGURE 5.2: Corrected yield for both mesons π^0 (top) η (bottom) for different multiplicity bins. Systematic uncertainties are shown as boxes and statistical uncertainties are drawn in vertical error bars.

R_{pPb} for both mesons at $\sqrt{s_{NN}} = 8\,\text{TeV}$ and $\sqrt{s_{NN}} = 5.2\,\text{TeV}$ is illustrated in figure 5.5 for π^0 and in figure 5.6 for η.

There is an agreement between the nuclear modification factor for π^0 and η. At high p_T the ratio is consistent with unity since, the N_{coll} scaling is satisfied due to the abundant energy to produce more particles. The yield is suppressed at low p_T and the number of binary collisions scaling is not satisfied.

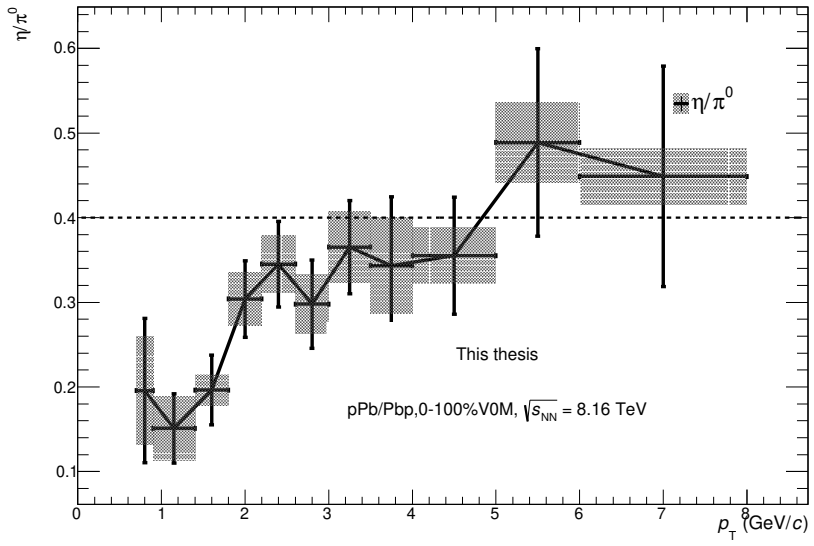

FIGURE 5.3: The ratio increases with pt and levels out at 0.4-0.5 for $p_T > 4\text{GeV/c}$

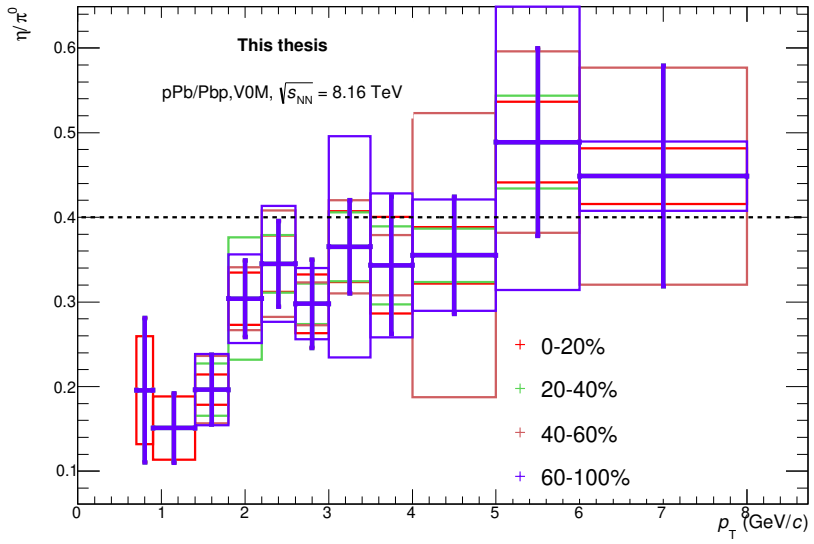

FIGURE 5.4: η to π^0 for different multiplicity bins. Systematic uncertainties are shown as boxes, statistical uncertainties shown as error bars.

The systematic uncertainties for the R_{pPb} ratio of p-Pb at $\sqrt{s_{NN}} = 8TeV$ are not calculated. For p-Pb at $\sqrt{s_{NN}} = 5.2TeV$ systematic uncertainties are drawn in vertical boxes. The difference between the two ratios is attributed to the fact that pp spectrum for $\sqrt{s_{NN}} = 5\,\text{TeV}$ is not available and the ratio has been calculated interpolating pp spectrum at $\sqrt{s_{NN}} = 2.76\,\text{TeV}, 7\,\text{TeV}$

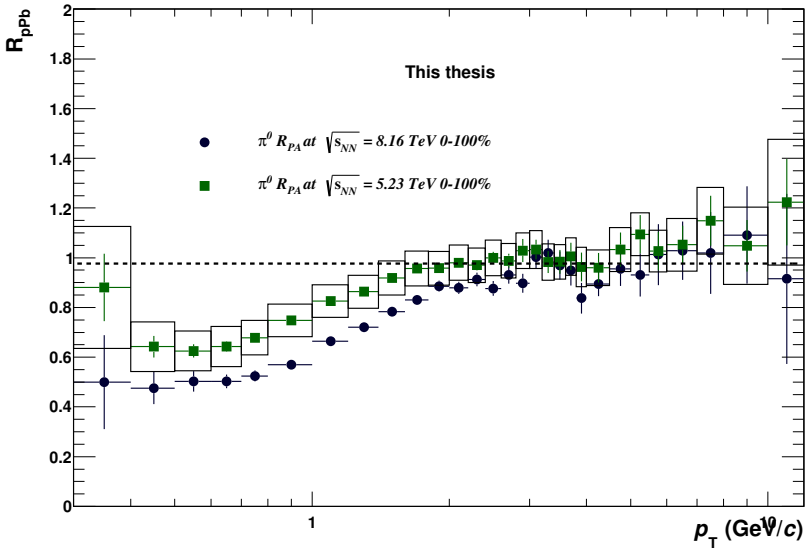

FIGURE 5.5: Nuclear modification factors for π^0 at $\sqrt{s_{NN}} = 5.2\,TeV$ in Green [64], and at $\sqrt{s_{NN}} = 8.16\,TeV$ in black. Systematic uncertainties are shown as boxes and statistical uncertainties are drawn as vertical error bars. No systematic uncertainties were calculated for the ratio at $\sqrt{s_{NN}} = 8.16\,TeV$

.

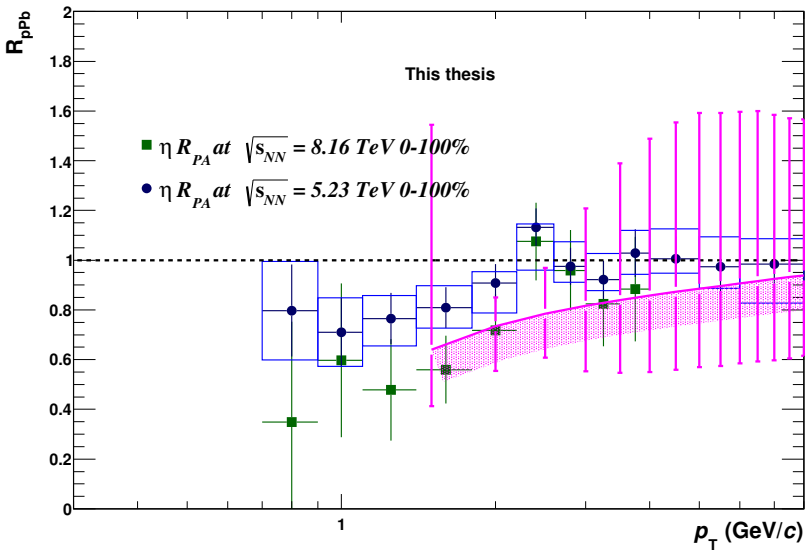

FIGURE 5.6: Nuclear modification factors for η at $\sqrt{s_{NN}} = 5.2\,\text{TeV}$ in Blue [64], and at $\sqrt{s_{NN}} = 8.16\,\text{TeV}$ in black. Systematic uncertainties are shown as boxes and statistical uncertainties are drawn as vertical error bars. No systematic uncertainties were calculated for the ratio at $\sqrt{s_{NN}} = 8.16\,\text{TeV}$

.

and 8 TeV. Another source of uncertainty between the two ratios is that same number of binary collisions has been used to calculate two different ratios at different energies. However, the ratio calculated for p-Pb at $\sqrt{s_{NN}} = 8\,TeV$ is more accurate since the reference is available in the same energy. In additionally, the integrated luminosity for pp at $\sqrt{s_{NN}} = 8$ TeV is factor of five higher than for $\sqrt{s_{NN}} = 5$ TeV [65].

5.2 Comparison to theoretical predictions

The measured experimental data of the neutral meson results presented in section 5 will be compared to theoretical model predictions. First, the neutral meson transverse momentum spectra compared to several theoretical calculations is shown in figure 5.7 and 5.8.

The NLO pQCD calculations presented in black color use the

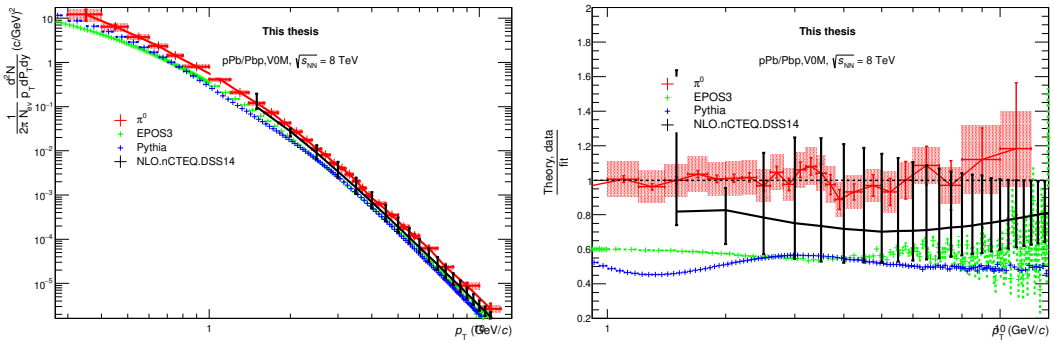

FIGURE 5.7: Invariant differential yield for π^0 compared to several Theoretical calculations.

nCTEQ nPDF [66], and the fragmentation function DSS14 [67]. This model is able to reproduce the π^0 invariant yield within uncertainties attributed to nPDF, the fragmentation function as well as the variation of the factorization and renormalization [64].

The measured meson yields are additionally compared to the PYTHIA8 [47] event generator, indicated in blue circles shown in right side of figure 5.8 the ratio of the data points and and theory models to the Tsallis fit of the spectrum. For π^0 the measured spectra is underestimated at all p_T ranges by factor of 0.4.

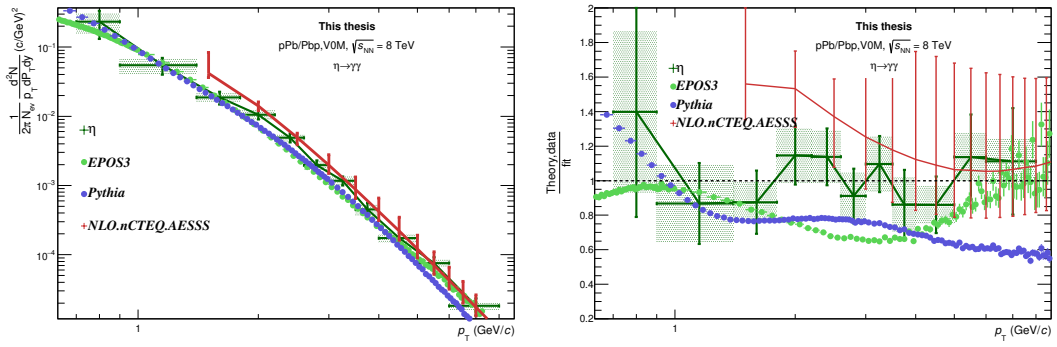

FIGURE 5.8: Invariant differential yield for η compared to several Theoretical calculations.

In comparison to EPOS3, the measured spectrum is reproduced with worse agreement to data at low p_T and at high p_T as illustrated in green in figure 5.8. The invariant yield for the η meson shown in figure 5.8 bottom is compared to pQCD calculations using nCTEQ nPDF and AESSS fragmentation function [68]. The calculation agrees with the data (green cross) within uncertainties. The spectra produced by EPOS3 [69] is underestimated at low p_T and agrees at high p_T. Additionally, in comparison to PYTHIA8 event generator, the spectra overestimated at low p_T nevertheless, agrees toward high p_T within uncertainties. The NLO pQCD (red cross) is the best production for the data since it agrees at a wider p_T range but, overestimates the spectra at high p_T. The theoretical models can also be compared to the η/π^0 ratio as shown in figure 5.9. The spectra for data is very limited in p_T due to the lack of statistics. The spectra produced by the generator PYTHIA8 (blue points)is consistent with data (black cross). For EPOS3 the predicted spectra are closer to spectra of data at low p_T while at high p_T EPOS3 calculation overestimates the η/π^0 ratio. The NLO pQCD calculation also overestimates the ratio over the whole p_T range.

Figure 5.10 shows the nuclear modification factor R_{pPb} for π^0 (top) and for η (bottom). measured in p-Pb collisions at $\sqrt{s_{NN}} = 8.16$ TeV in comparison to several theoretical calculations. First, NLO pQCD calculation for π^0 using EPPS16 nPDF [70] are indicated in blue. The NLO calculation underestimates the measured nuclear modification factors for low transverse momenta.

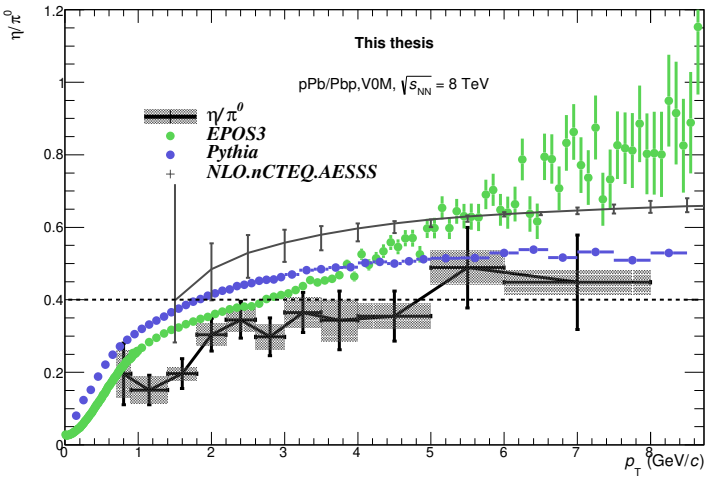

FIGURE 5.9: η/π^0 ratio compared to theoretical calculations.

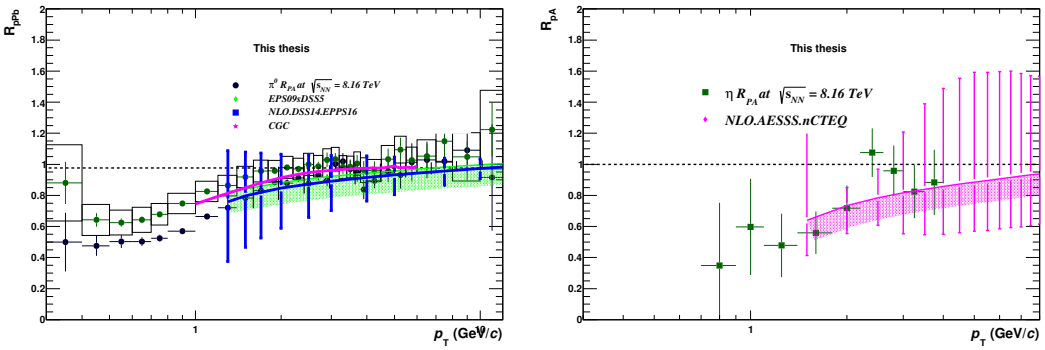

FIGURE 5.10: Nuclear modification factors for π^0 (left) and η (right) compared to theoretical calculations.

At high p_T the calculations agree with data. The CGC calculation [71] is able to reproduce the neutral pion modification factor with some discrepancy.
This comparison indicates that theoretical calculations can reproduce the data. Further, it shows that models agree better to the neutral pion π^0 measurement than to the η measurement.

Chapter 6

Conclusion

The measurement of the neutral mesons, π^0 and η, by using the photon Conversion method in $p-pPb$ collisions at $\sqrt{s_{NN}} = 8.16TeV$ with the ALICE detector. The two converted photon decay channels of both mesons are reconstructed in the central barrel of the ALICE detector. The invariant mass of neutral mesons is calculated by combining the two photons candidates then, reconstructed on statistical basis since they appear as an excess on their respective mass. The spectra is corrected using Monte Carlo simulations with the DPMJet and EPOS event generators. The invariant yield of both mesons is measured as well as the η/π^0 ratio for minimum bias collisions and different multiplicity classes. The ratio does not show multiplicity dependence. The nuclear modification factor is calculated for minimum bias collisions. It shows consistency with unity at high p_{T} and deviation from unity at low p_{T} that indicates particle suppression due to nuclear effects.
All the above quantities are compared to predictions form theoretical models like NLO pQCD calculations, event generators and Color Glass condensate calculation. All models reproduce the measured spectra for π^0 and for η within uncertainties. A clear statement about which model is the best to reproduce data is not possible since their uncertainties are not available.
The measurement of neutral mesons serves as an important input for theoretical models,hence, to be able to constrain nuclear parton distribution functions and fragmentation functions.

Appendix A

Appendix

Appendix A

A.1 Invariant mass distributions

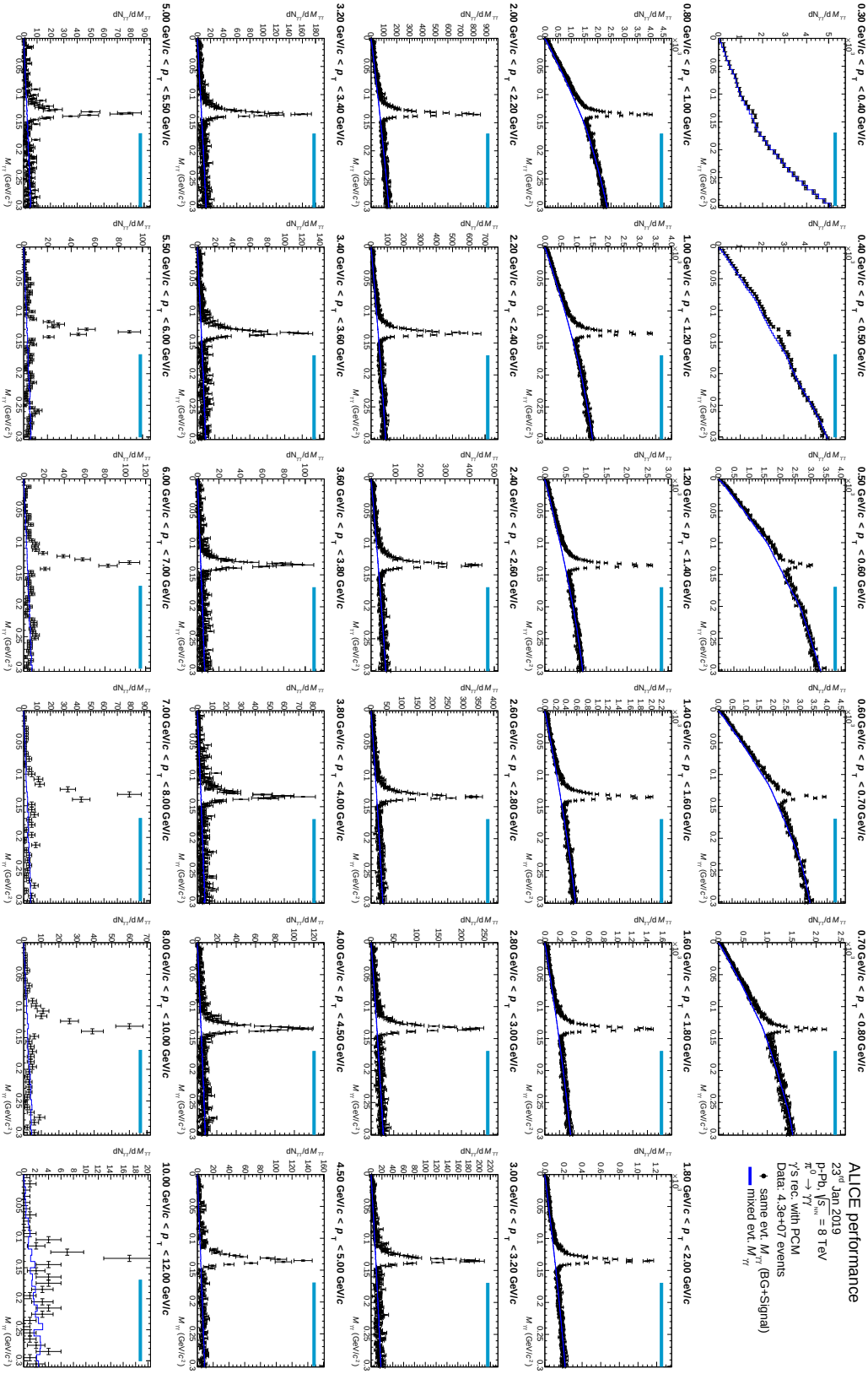

FIGURE A.1: π^0 Invariant mass distributions before subtracting the combinatorial background

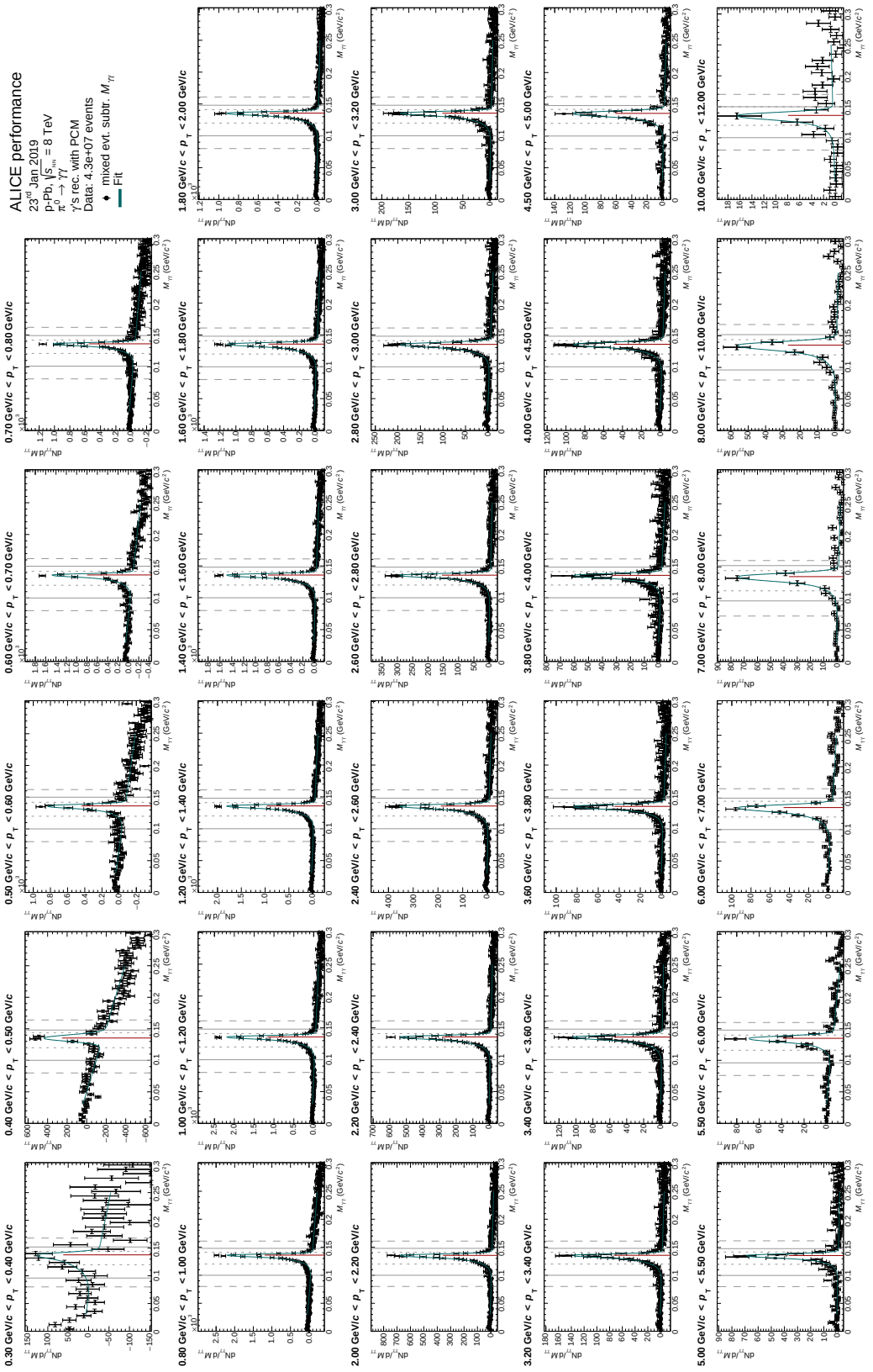

FIGURE A.2: π^0 Invariant mass distributions after subtracting the combinatorial background

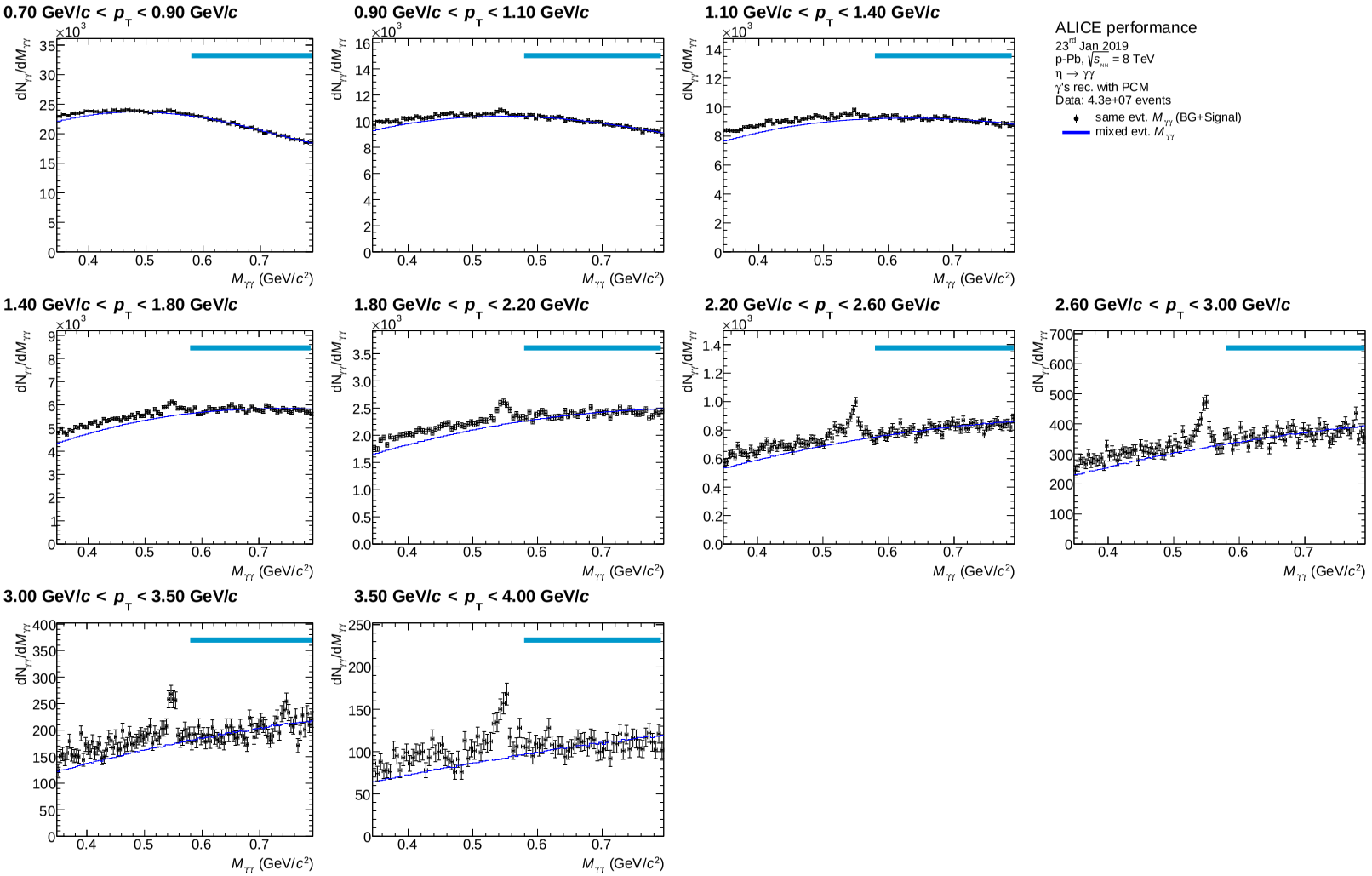

FIGURE A.3: η Invariant mass distributions before subtracting the combinatorial background

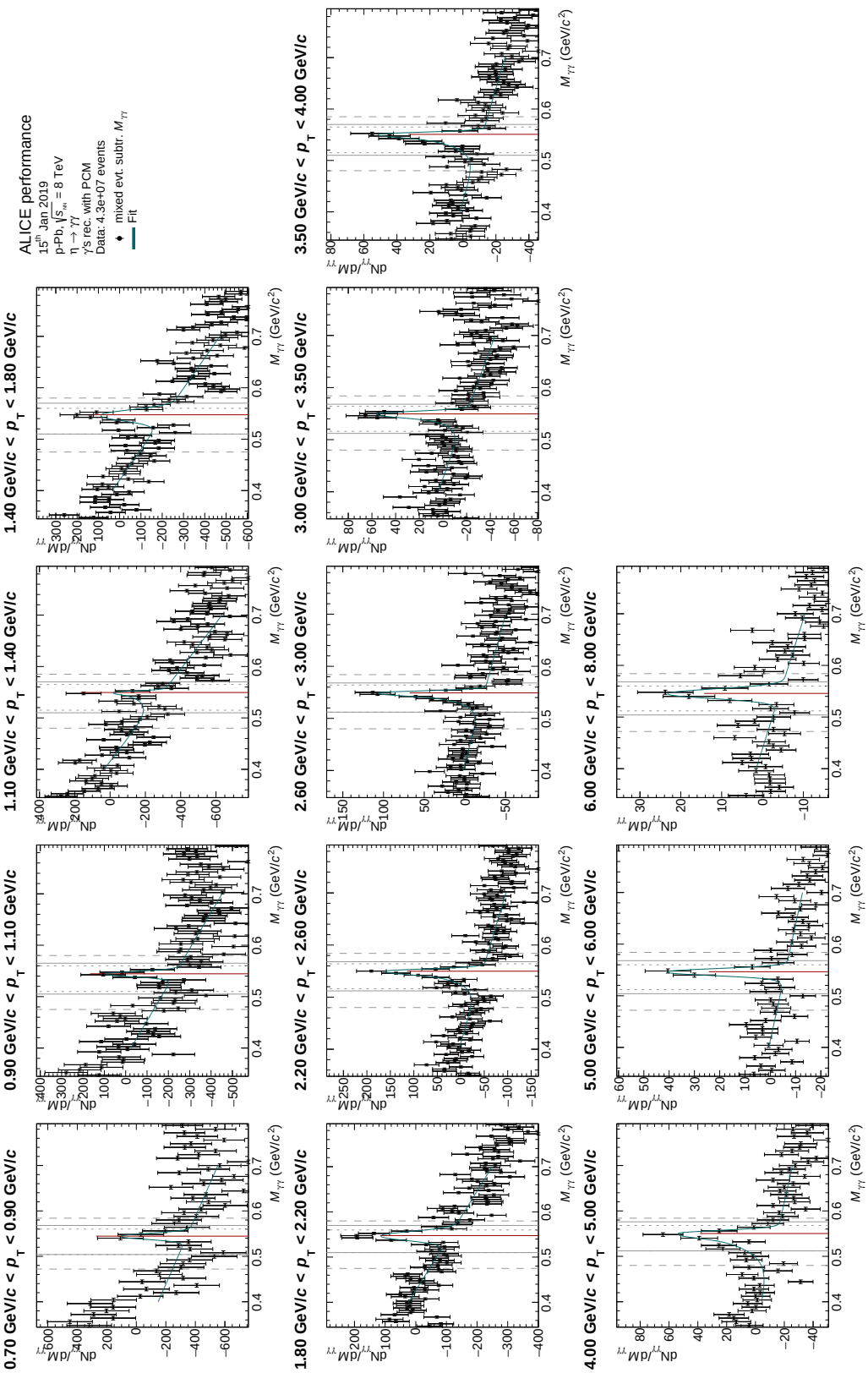

FIGURE A.4: η Invariant mass distributions after subtracting the combinatorial background

Appendix B

Appendix

B.1 Correction factor for different multiplicity bins

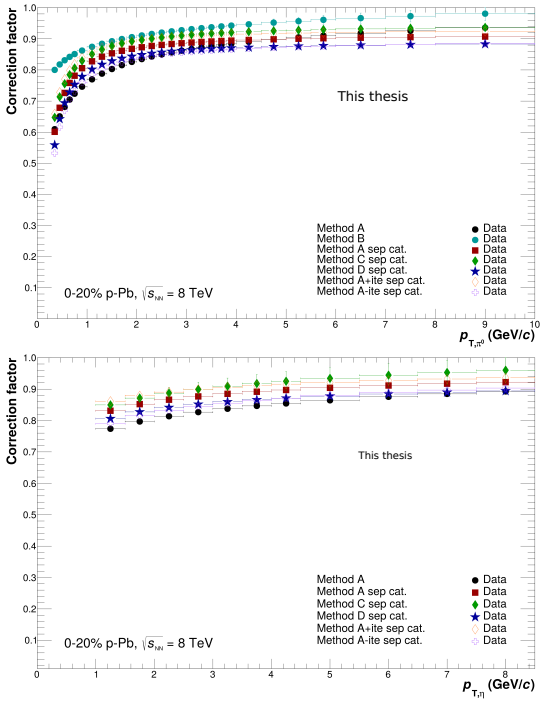

FIGURE B.1: Correction factor for π^0 to (left) and for η to right for multiplicity bin 0-20%. Method A sep cat used for this analysis.

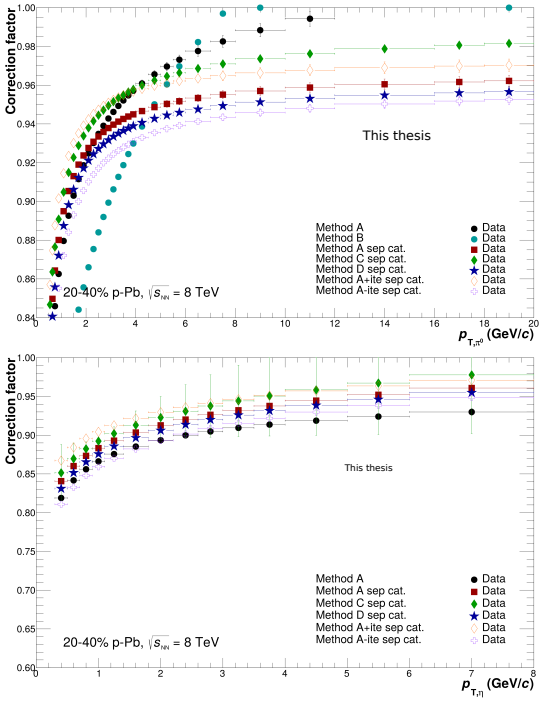

FIGURE B.2: Correction factor for π^0 to (left) and for η to right for multiplicity bin 20-40%. Method A sep cat used for this analysis.

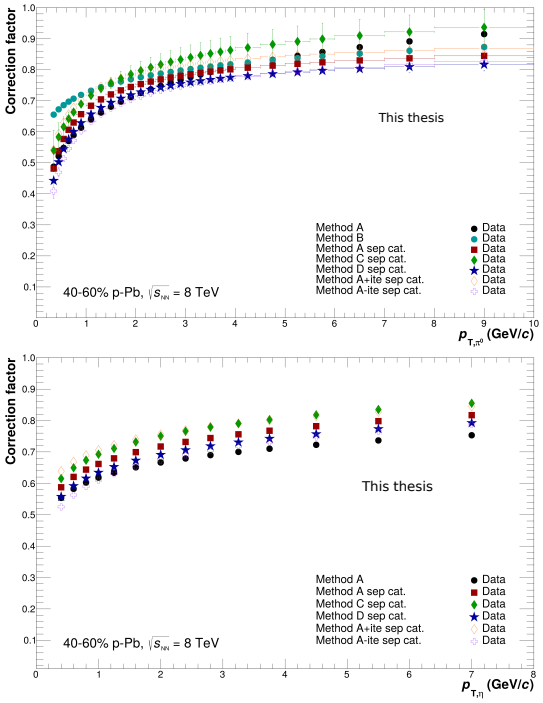

FIGURE B.3: Correction factor for π^0 to (left) and for η to right for multiplicity bin 40-60%. Method A sep cat used for this analysis.

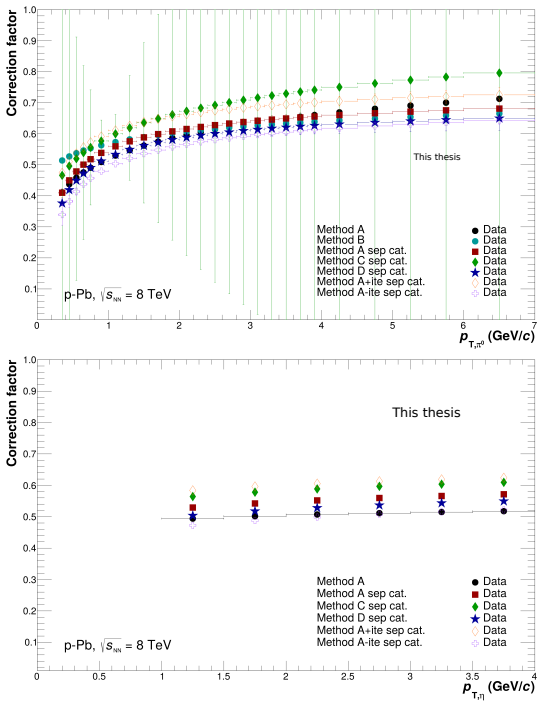

FIGURE B.4: Correction factor for π^0 to (left) and for η to right for multiplicity bin 60-100%. Method A sep cat used for this analysis.

Appendix C

Appendix

C.1 η / π^0 ratio for different multiplicities

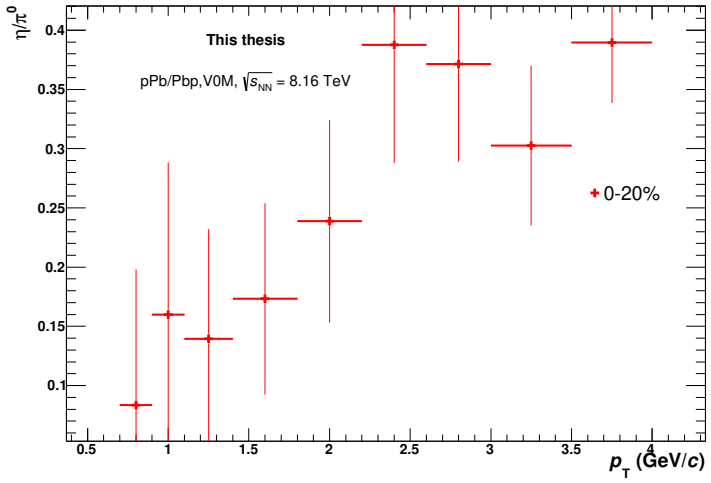

FIGURE C.1: η / π^0 ratio for different multiplicities.

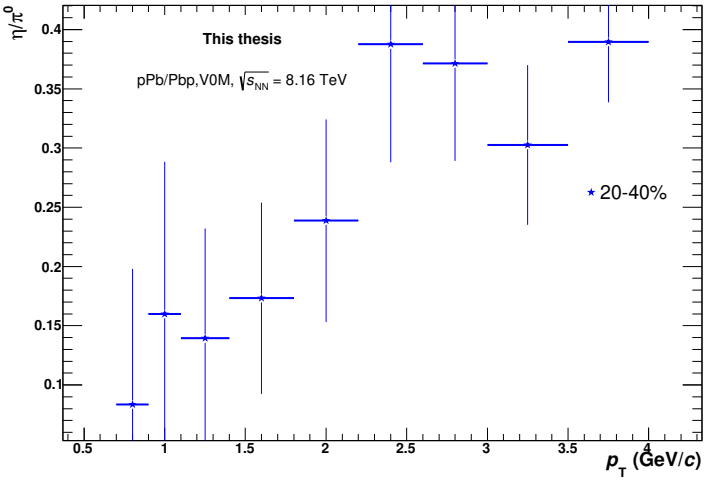

FIGURE C.2: η/π^0 ratio for different multiplicities.

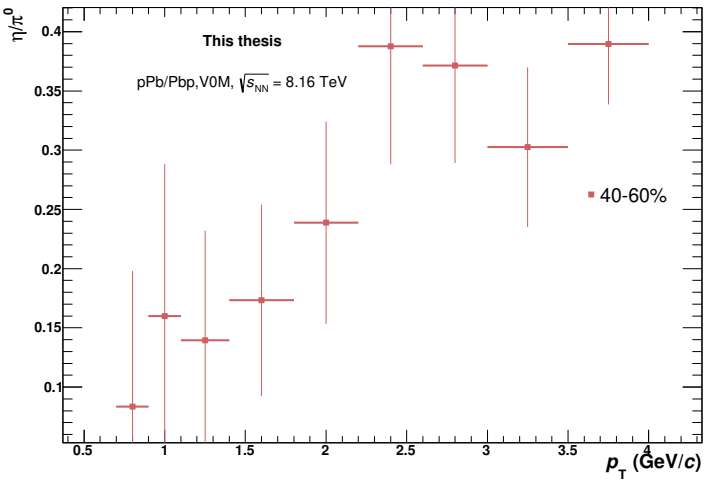

FIGURE C.3: η/π^0 ratio for different multiplicities.

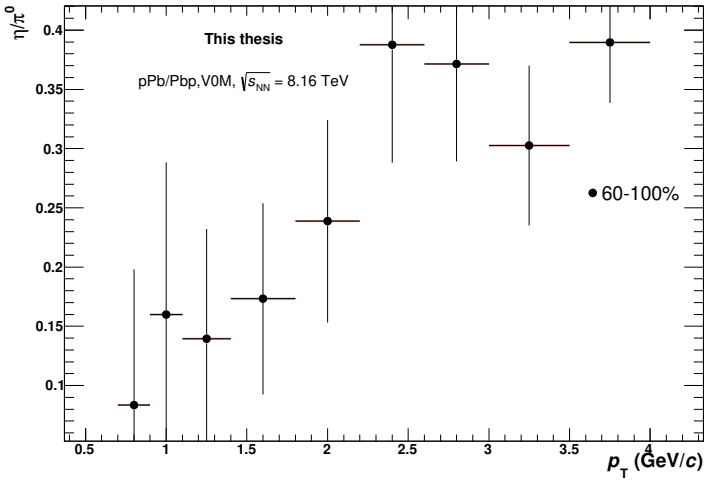

FIGURE C.4: η/π^0 ratio for different multiplicities.

Appendix D

Appendix

D.1 Interpolated pp spectrum for both mesons

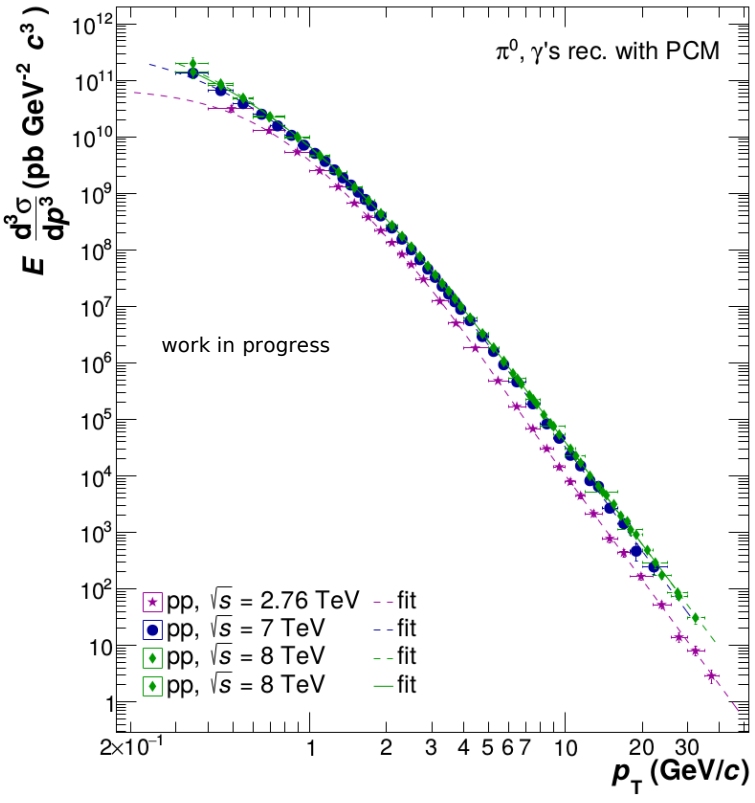

FIGURE D.1: Interpolated π^0 pp spectrum, produced by the PCM group.

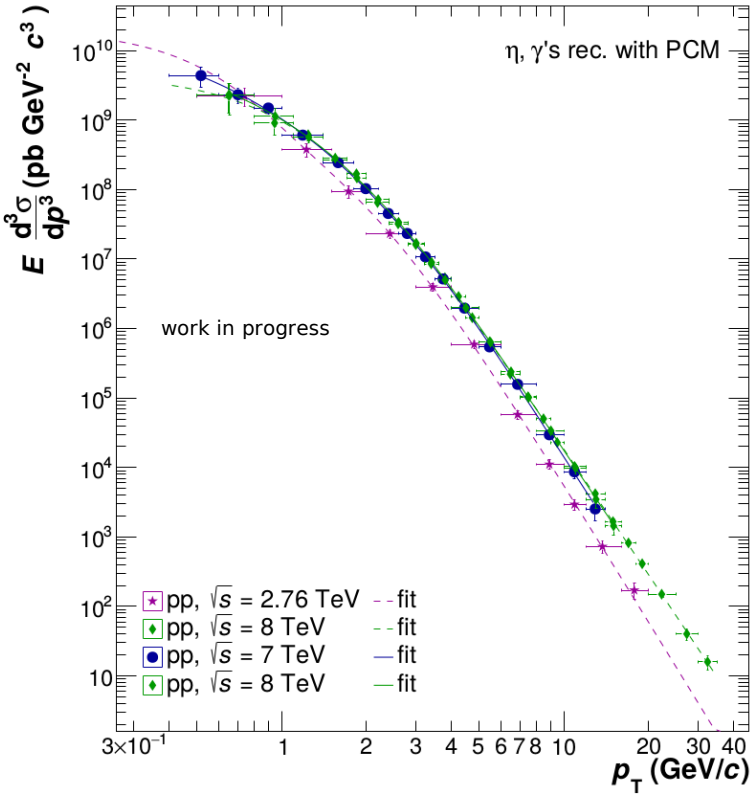

FIGURE D.2: Interpolated η pp spectrum, produced by the PCM group

References

[1] C. De Melis, "The CERN accelerator complex. Complexe des accélérateurs du CERN," Jan 2016. General Photo.

[2] J. Adam and Adamov, "*d*-meson production in *p*-Pb collisions at $\sqrt{s_{NN}} = 5.02$ tev and in *pp* collisions at $\sqrt{s} = 7$ tev," *Phys. Rev. C*, vol. 94, p. 054908, Nov 2016.

[3] C. A. Salgado *et al.*, "Proton-Nucleus Collisions at the LHC: Scientific Opportunities and Requirements," *J. Phys.*, vol. G39, p. 015010, 2012.

[4] T. Peitzmann and M. H. Thoma, "Direct photons from relativistic heavy ion collisions," *Phys. Rept.*, vol. 364, pp. 175–246, 2002.

[5] A. M. ALICE collaboration, "Neutral pion and eta meson measurements with the alice detector," *Journal of Physics: Conference Series*, vol. 832, no. 1, p. 012011, 2017.

[6] N. Schmidt, ""neutral meson and direct photon measurements with conversions in alice in proton-proton collisions at sqrt(s) = 0.9, 7 and 8 tev"," *"University of Heidelberg."*, vol. "MasterThesis", "2017".

[7] R. J. "Fries and B. Muller, "Heavy ions at LHC: Theoretical issues," *"Eur. Phys. J."*, vol. "C34", pp. "S279–S285", "2004".

[8] K. "Yagi, T. Hatsuda, and Y. Miake, "Quark-gluon plasma: From big bang to little bang," *"Camb. Monogr. Part. Phys. Nucl. Phys. Cosmol."*, vol. "23", pp. "1–446", "2005".

[9] F. Karsch, "Lattice QCD at high temperature and density," *Lect. Notes Phys.*, vol. 583, pp. 209–249, 2002.

[10] E. V. "Shuryak, "What RHIC experiments and theory tell us about properties of quark-gluon plasma?," *"Nucl. Phys."*, vol. "A750", "2005".

[11] R. "Snellings, "Elliptic Flow: A Brief Review," "*New J. Phys.*", vol. "13", p. "055008", "2011".

[12] C. Shen, U. Heinz, P. Huovinen, and H. Song, "Radial and elliptic flow in Pb+Pb collisions at the Large Hadron Collider from viscous hydrodynamic," *Phys. Rev.*, vol. C84, p. 044903, 2011.

[13] F. Becattini, "An Introduction to the Statistical Hadronization Model," in *International School on Quark-Gluon Plasma and Heavy Ion Collisions: past, present, future Villa Gualino, Torino, Italy, December 8-14, 2008*, 2009.

[14] J. D. "Bjorken, "Highly Relativistic Nucleus-Nucleus Collisions: The Central Rapidity Region," "*Phys. Rev.*", vol. "D27", pp. "140–151", "1983".

[15] M. Wilde, *Measurement of Direct Photons in pp and Pb–Pb Collisions with Conversion Pairs*. PhD thesis, U. Munster, 2015.

[16] B. Muller, J. Schukraft, and B. Wyslouch, "First Results from Pb+Pb collisions at the LHC," *Ann. Rev. Nucl. Part. Sci.*, vol. 62, pp. 361–386, 2012.

[17] E. Schnedermann, J. Sollfrank, and U. W. Heinz, "Thermal phenomenology of hadrons from 200-A/GeV S+S collisions," *Phys. Rev.*, vol. C48, pp. 2462–2475, 1993.

[18] S. "Voloshin and Y. Zhang, "Flow study in relativistic nuclear collisions by Fourier expansion of Azimuthal particle distributions," "*Z. Phys.*", vol. "C70", pp. "665–672", "1996".

[19] K. Aamodt *et al.*, "Higher harmonic anisotropic flow measurements of charged particles in Pb-Pb collisions at $\sqrt{s_{NN}}$=2.76 TeV," *Phys. Rev. Lett.*, vol. 107, p. 032301, 2011.

[20] U. Heinz, C. Shen, and H. Song, "The viscosity of quark-gluon plasma at RHIC and the LHC," *AIP Conf. Proc.*, vol. 1441, pp. 766–770, 2012.

[21] D. H. Rischke, "The Quark gluon plasma in equilibrium," *Prog. Part. Nucl. Phys.*, vol. 52, pp. 197–296, 2004.

[22] K. J. Eskola, H. Paukkunen, and C. A. Salgado, "EPS09: A New Generation of NLO and LO Nuclear Parton Distribution Functions," *JHEP*, vol. 04, p. 065, 2009.

[23] N. Armesto, "Nuclear shadowing," *J. Phys.*, vol. G32, pp. R367–R394, 2006.

[24] Y. Mehtar-Tani and G. Wolschin, "Baryon stopping and saturation physics in relativistic collisions," *Phys. Rev.*, vol. C80, p. 054905, 2009.

[25] A. Accardi, "Cronin effect in proton nucleus collisions: A Survey of theoretical models," 2002.

[26] B. M. K. Nefkens and J. W. Price, "The Neutral decay modes of the eta meson," *Phys. Scripta*, vol. T99, pp. 114–122, 2002.

[27] A. Majumder and M. Van Leeuwen, "The Theory and Phenomenology of Perturbative QCD Based Jet Quenching," *Prog. Part. Nucl. Phys.*, vol. 66, pp. 41–92, 2011.

[28] F. Bock", ""alice capabilities for studying photon physics with the conversion method at lhc energies",," *"University of Heidelberg."*, vol. "bachelorthesis", "June 2010".

[29] M. M. Aggarwal *et al.*, "Direct photon production in 158-A-GeV Pb-208 + Pb-208 collisions," 2000.

[30] C. P. Burgess, "Goldstone and pseudoGoldstone bosons in nuclear, particle and condensed matter physics," *Phys. Rept.*, vol. 330, pp. 193–261, 2000.

[31] M. Cheng *et al.*, "The Transition temperature in QCD," *Phys. Rev.*, vol. D74, p. 054507, 2006.

[32] G. A. ATLAS Collaboration, "The CMS Experiment at the CERN LHC," *JINST*, vol. 3, p. S08005, 2008.

[33] S. Chatrchyan *et al.*, "The CMS Experiment at the CERN LHC," *JINST*, vol. 3, p. S08004, 2008.

[34] F. C. W. ALICE Collaboration *et al.*, "ALICE: Physics performance report, volume II," *J. Phys.*, vol. G32, pp. 1295–2040, 2006.

[35] A. K. ALICE Collaboration *et al.*, "The ALICE experiment at the CERN LHC," *JINST*, vol. 3, p. S08002, 2008.

[36] A. B. ALICE Collaboration *et al.*, "Performance of the ALICE Experiment at the CERN LHC," *Int. J. Mod. Phys.*, vol. A29, p. 1430044, 2014.

[37] P. C. e. a. ALICE Collaboration, "ALICE forward detectors: FMD, TO and VO: Technical Design Re- port. Technical Design Report ALICE. Submitted on 10 Sep 2004. Geneva: CERN,, volume II," *J. Phys.*, vol. G32, pp. 1295–2040, 2004.

[38] A. E. ALICE Collaboration *et al.*, "Performance of the ALICE VZERO system," *JINST*, vol. 8, p. P10016, 2013.

[39] D. G. ALICE Collaboration *et al.*, "ALICE technical design report of the inner tracking system (ITS)," 1999.

[40] A. K. ALICE Collaboration *et al.*, "Alignment of the ALICE Inner Tracking System with cosmic-ray tracks," *JINST*, vol. 5, p. P03003, 2010.

[41] A. K. ALICE Collaboration *et al.*, "The ALICE TPC, a large 3-dimensional tracking device with fast readout for ultra-high multiplicity events"," *JINST*, vol. 5, p. P03003, 2010.

[42] A. ALICE Collaboration, ""http://aliceinfo.cern.ch/.",,"

[43] D. G. ALICE Collaboration *et al.*, "ALICE technical design report of the photon spectrometer (PHOS)," 1999.

[44] A. ATLAS Collaboration, ""http://atlas.ch/",,"

[45] R. condition table, ""url: https://alimonitor.cern.ch/configuration/",,"

[46] C. a C language family frontend for LLVM., ""url: http://clang.llvm.org/.",,"

[47] T. Sjöstrand, S. Ask, J. R. Christiansen, R. Corke, N. Desai, P. Ilten, S. Mrenna, S. Prestel, C. O. Rasmussen, and P. Z. Skands, "An Introduction to PYTHIA 8.2," *Comput. Phys. Commun.*, vol. 191, pp. 159–177, 2015.

[48] M. Gyulassy and X.-N. Wang, "HIJING 1.0: A Monte Carlo program for parton and particle production in high-energy hadronic and nuclear collisions," *Comput. Phys. Commun.*, vol. 83, p. 307, 1994.

[49] S. Roesler, R. Engel, and J. Ranft, "The Monte Carlo event generator DPMJET-III," in *Advanced Monte Carlo for radiation physics, particle transport simulation and applications. Proceedings, Conference, MC2000, Lisbon, Portugal, October 23-26, 2000*, pp. 1033–1038, 2000.

[50] T. "Pierog, I. Karpenko, J. M. Katzy, E. Yatsenko, and K. Werner, "EPOS LHC: Test of collective hadronization with data measured at the CERN Large Hadron Collider," *"Phys. Rev."*, vol. "C92", no. "3", p. "034906", "2015".

[51] R. Brun, R. Hagelberg, M. Hansroul, and J. C. Lassalle, *Simulation program for particle physics experiments, GEANT: user guide and reference manual*. Geneva: CERN, 1978.

[52] P. c. g. "ALICE Collaboration

[53] A. w. "ALICE Collaboration

[54] ""the coordinated theoretical-experimental project on qcd","

[55] R. Frühwirth, "Application of kalman filtering to track and vertex fitting," *Nuclear Instruments and Methods in Physics Research Section A: Accelerators, Spectrometers, Detectors and Associated Equipment*, vol. 262, no. 2, pp. 444 – 450, 1987.

[56] A. Capella, U. Sukhatme, C.-I. Tan, and J. T. T. Van, "Dual parton model," *Physics Reports*, vol. 236, no. 4, pp. 225 – 329, 1994.

[57] H. J. Drescher, M. Hladik, S. Ostapchenko, T. Pierog, and K. Werner, "Parton based Gribov-Regge theory," *Phys. Rept.*, vol. 350, pp. 93–289, 2001.

[58] A. B. B. ALICE Collaboration *et al.*, "Neutral pion production at midrapidity in pp and Pb-Pb collisions at $\sqrt{s_{\mathrm{NN}}} = 2.76\,\mathrm{TeV}$," *Eur. Phys. J.*, vol. C74, no. 10, p. 3108, 2014.

[59] S. Gorbunov and I.Kisel, "Alikfparticle package."

[60] S.Gorbunov and I.Kisel2, "Reconstruction of decayed particles based on the kalman filter", year = 2007 reportnumber =,"

[61] S. Gorbunov and I.Kisel, "Analysis of v-events", year = 1954 =,"

[62] A. Passfeld", ""neutral meson measurement via photon conversions in p-pb collisions at sqrt(s)= 5.02 tev with alice at the lhc",", vol. "ALICE Analysis Note.", "2014".

[63] C.-Y. Wong and G. Wilk, "Tsallis fits to p_T spectra and multiple hard scattering in pp collisions at the LHC," *Phys. Rev.*, vol. D87, no. 11, p. 114007, 2013.

[64] A. S. ALICE Collaboration *et al.*, "Neutral pion and η meson production in p-Pb collisions at $\sqrt{s_{\rm NN}} = 5.02$ TeV," *Eur. Phys. J.*, vol. C78, no. 8, p. 624, 2018.

[65] J. L. al", ""predictions for cold nuclear matter effects in p+pb collisions at snn=8.16 tev"," *"Nuclear Physics A"*, vol. "972", pp. "18 – 85", "2018".

[66] K. Kovarik *et al.*, "nCTEQ15 - Global analysis of nuclear parton distributions with uncertainties in the CTEQ framework," *Phys. Rev.*, vol. D93, no. 8, p. 085037, 2016.

[67] D. de Florian, R. Sassot, M. Epele, R. J. Hernández-Pinto, and M. Stratmann, "Parton-to-Pion Fragmentation Reloaded," *Phys. Rev.*, vol. D91, no. 1, p. 014035, 2015.

[68] C. A. Aidala, F. Ellinghaus, R. Sassot, J. P. Seele, and M. Stratmann, "Global Analysis of Fragmentation Functions for Eta Mesons," *Phys. Rev.*, vol. D83, p. 034002, 2011.

[69] K. Werner, B. Guiot, I. Karpenko, and T. Pierog, "Analysing radial flow features in p-Pb and p-p collisions at several TeV by studying identified particle production in EPOS3," *Phys. Rev.*, vol. C89, no. 6, p. 064903, 2014.

[70] K. J. Eskola, P. Paakkinen, H. Paukkunen, and C. A. Salgado, "EPPS16: Nuclear parton distributions with LHC data," *Eur. Phys. J.*, vol. C77, no. 3, p. 163, 2017.

[71] T. Lappi and H. Mäntysaari, "Single inclusive particle production at high energy from HERA data to proton-nucleus collisions," *Phys. Rev.*, vol. D88, p. 114020, 2013.

[72] J.-Y. Ollitrault", ""anisotropy as a signature of transverse collective flow"," *"Phys. Rev. D 46 Jul 229-245."*, "1992".

[73] N. K. Particle Data Group Collaboration *et al.*, "Review of particle physics," *J. Phys.*, vol. G37, p. 075021, 2010.

[74] M. G. Alford, A. Schmitt, K. Rajagopal, and T. Schäfer, "Color superconductivity in dense quark matter," *Rev. Mod. Phys.*, vol. 80, pp. 1455–1515, 2008.

[75] A. Matyja, M. Kowalski, D. Roehrich, D. T. Larsen, D. Fehlker, H. Helstrup, B. Sitar, M. Pikna, M. Siska, R. Janik, P. Strmen, I. Szarka, L. Musa, C. Lippmann, M. Mager, A. U Rehman, S. Rossegger, B. S Nielsen, C. Soegaard, and C. , "Alice tpc-design and performance," *Proceedings of Science*, 01 2009.

[76] F. Bock, ""neutral pion and eta meson production in pp and pb–pb collisions at the lhc with the alice detector"," *"University of Heidelberg."*, vol. "Master's thesis", "December 2012".

[77] N. Schmidt, ""neutral meson measurements with the photon conversion method in alice in pp collisions at sqrt(s)=8 tev"," vol. "ALICE Analysis Note.", "2016".